

Lab on a Chip

Devices and applications at the micro- and nanoscale

Accepted Manuscript

This article can be cited before page numbers have been issued, to do this please use: M. S. Khan, M. Ali, Y. B. Bang, S. J. Lee and J. Park, *Lab Chip*, 2026, DOI: 10.1039/D6LC00140H.



This is an Accepted Manuscript, which has been through the Royal Society of Chemistry peer review process and has been accepted for publication.

Accepted Manuscripts are published online shortly after acceptance, before technical editing, formatting and proof reading. Using this free service, authors can make their results available to the community, in citable form, before we publish the edited article. We will replace this Accepted Manuscript with the edited and formatted Advance Article as soon as it is available.

You can find more information about Accepted Manuscripts in the [Information for Authors](#).

Please note that technical editing may introduce minor changes to the text and/or graphics, which may alter content. The journal's standard [Terms & Conditions](#) and the [Ethical guidelines](#) still apply. In no event shall the Royal Society of Chemistry be held responsible for any errors or omissions in this Accepted Manuscript or any consequences arising from the use of any information it contains.

Acoustofluidic Separation of Oblate Spheroid from Sphere using Acoustic Radiation Torque and Force

View Article Online
DOI: 10.1039/C6LC00140H

Muhammad Soban Khan,¹ Mushtaq Ali,¹ Yong Bin Bang,² Seong Jae Lee^{2,*} and Jinsoo Park^{1,*}

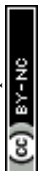
¹Department of Mechanical Engineering, Chonnam National University, 77 Yongbong-ro, Buk-gu, Gwangju 61186, Republic of Korea

²Department of Polymer Engineering, The University of Suwon, 17 Wauan-gil, Bongdam-eup, Hwaseong, Gyeonggi 18323, Republic of Korea

*Correspondence: Jinsoo Park (jinsoopark@jnu.ac.kr) and Seong Jae Lee (sjlee@suwon.ac.kr)

Abstract

Cells, bacteria, and other bioparticles exist in diverse shapes, and their morphology plays a pivotal role in biological functions and clinical significance. Various microfluidic approaches have been developed for shape-based separation of bioparticles with the same or similar volume; however, most of them were limited to separation of prolate spheroids from spheres or required a priori labeling and consequent detection. Here, we propose a vertical-type acoustofluidic method for the first separation of oblate spheroid from sphere in a label-free manner. The acoustic radiation torque suppresses the rotational motion of the oblate micro-objects, leading to horizontal alignment with an increase in projected surface area compared to that of the isovolumetric spheres. The enhanced acoustic radiation force, proportional to the projected surface area normal to the wave propagation, allows the oblate spheroids to have greater vertical migration inside a microchannel, resulting in distinct trajectories for the shape-based separation. We conduct numerical simulations of asymmetric wave scattering to elucidate the working principle and experiments to demonstrate the separation of polystyrene microparticles and red blood cells of spherical and oblate shapes at high purity and recovery rate. The proposed acoustofluidic approach holds promise for label-free, shape-based manipulation of bioparticles in cell biology and microbiology.



1. Introduction

View Article Online
DOI: 10.1039/D6LC00140H

Cells, bacteria, and other bioparticles exhibit diverse shapes that significantly influence their biological functions and clinical relevance.(1-4) Human cells exhibit a diverse range of shapes that are crucial for their functions: for instance, immune functions of macrophages,(5) epithelial-to-mesenchymal cancer cell progression,(6) and metastatic potential of tumor cells.(7) Specifically, human red blood cells (RBCs) exhibit a characteristic biconcave shape, with a diameter of 6–8 μm under healthy conditions, which enhances their flexibility and oxygen exchange efficiency.(8, 9) Alterations in RBC morphology are closely associated with pathological conditions, often leading to changes in mechanical properties and reduced oxygen-carrying capacity.(10) For example, malaria-infected RBCs transform from their native biconcave shape into a more spherical form,(11) while hereditary spherocytosis also results in spherical RBCs due to membrane defects.(12) Elongated or elliptical RBCs are associated with elliptocytosis,(10) whereas sickle or crescent-shaped RBCs are characteristic of sickle cell disease.(13) In addition, teardrop-shaped RBCs are indicative of myelofibrosis.(14) Therefore, the ability to identify and separate bioparticles based on shape is of significant importance for biomedical diagnostics, disease monitoring, and therapeutic assessment.(15, 16)

Various microfluidic approaches have been proposed for shape-based bioparticle manipulation with advantages including precise, non-invasive processing, reduced reagent consumption, versatility, and easy integration.(17-19) A few successful demonstrations include inertial microfluidics for separation of spherical and rod-shaped *Euglena gracilis* microalgae,(20, 21) deterministic lateral displacement for separation of biconcave RBCs and elongated *T. cyclops* parasite,(22, 23) and hydrodynamic filtration for separation of erythrocytes blood leukocytes.(24) These approaches primarily rely on flow-induced hydrodynamic effects and often require precise channel geometries or specific flow conditions for effective separation. In contrast, acoustofluidic techniques enable contactless and label-free manipulation of non-spherical particles based on acoustic radiation torque (ART) and acoustic radiation force (ARF), allowing dynamic control over particle orientation and trajectory. In standing bulk acoustic wave(25-27) and standing surface acoustic wave(28, 29) ART has been shown to suppress rotational motion of prolate spheroids, leading to orientation-dependent focusing. Building on this, we previously demonstrated the separation of the prolate spheroids from isovolumetric microspheres in a travelling surface acoustic wave (TSAW) field.(30) However, these approaches have been largely limited to prolate–sphere separation. In such cases, ART-induced alignment reduces the projected surface area, resulting in weaker ARF. In contrast, the present work focuses on oblate spheroids, where alignment increases the projected surface area, leading



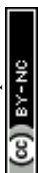
to enhanced ARF and distinct migration behavior. A comprehensive overview of these techniques can be found in our recent review.^(19, 31)

Here, we present a vertical-type acoustofluidic platform that enables, to the best of our knowledge, the first shape-based separation of oblate spheroids from isovolumetric spheres in a contactless and label-free manner, achieved through the combined effects of TSAW-induced ART and ARF. In the vertical-type configuration, the vertical wave propagation, whose magnitude is approximately 2.5 times greater than horizontal counterpart, is primarily utilized for separation of spherical and oblate micro-objects with enhanced separation efficiency and improved operational robustness. The TSAW-induced ART causes horizontal alignment of the oblate spheroids with an increase in the projected surface area normal to the wave propagation. The enhanced ARF on the oblate spheroids in the vertical direction due to the increased projected area allows their trajectory vertically shifted from the trajectory of the microspheres, leading to shape-based separation. We performed numerical simulations of wave scattering from oblate spheroids with varying orientation and aspect ratio (AR) to elucidate that the TSAW-induced ART and ARF are attributed to the asymmetric wave scattering. We also experimentally proved that the acoustic streaming effect is negligible to the acoustofluidic shape-based separation in the proposed platform. Based on the findings, we report the first demonstration of the shape-based separation of oblate and spherical polystyrene (PS) microparticles and RBCs at high purity and recovery rate of ~100%. We expect that the proposed acoustofluidic shape-based separation method holds promise in various fields including cell biology and microbiology.

2. Results and Discussion

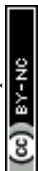
2.1 Device configuration

The proposed vertical-type acoustofluidic device consists of a straight interdigital transducer (IDT) on a piezoelectric lithium niobate (LiNbO_3) substrate with a polydimethylsiloxane (PDMS) microchannel with four inlets and two outlets, as shown in Fig. 1a. Suspended particles or cells were introduced through Inlet 1 at a flow rate of 50 $\mu\text{l/hr}$ and directed downward using a vertical sheath flow of 200 $\mu\text{l/hr}$ from Inlet 2, guiding them closer to the IDT. The suspensions were then sandwiched between two additional horizontal sheath flows from Inlets 3 and 4, each at a flow rate of 100 $\mu\text{l/hr}$, to achieve horizontal alignment. Unless otherwise specified, these flow rates were maintained for all experiments, resulting in a throughput of approximately 30–40 cells/s under the present operating conditions. It should be noted that the primary objective of this study is to demonstrate shape-based separation driven by the combined effects of ART



and ARF, rather than to achieve high-throughput performance. The throughput can be further improved through optimization of flow conditions and device design parameters. TSAWs generated by the IDT underneath the microchannel refract into the fluid at the Rayleigh angle ($\sim 22^\circ$ for $\text{LiNbO}_3/\text{water}$ interface), forming leaky longitudinal waves (LWs) within the channel. These acoustic waves induce both ART and ARF, leading to shape-dependent particle behaviors. Specifically, the ART arising from asymmetric side scattering promotes horizontal alignment of oblate spheroids. The ARF originates from asymmetries in forward and backward scattering on the horizontally aligned oblate spheroids (red in Fig. 1b) is greater than that exerted on the spheres (green in Fig. 1b) and thus drives further vertical migration of the oblate particles and cells. For direct observation of the vertical migration, we developed three-dimensional downstream bifurcation, which converts the two vertically distinguished particle trajectories into the horizontal ones. However, because the vertical particle migration is inherently difficult to visualize directly through standard inverted or upright microscopy, we also embedded a prism mirror at the side of the microchannel.(32) This prism optically redirects the side view of the vertical particle trajectories into the microscopes imaging plane, allowing real-time visualization and direct confirmation of the vertical separation process during operation.

For electrical isolation of the fluidic region from the IDT electrodes while preserving acoustic coupling, a thin PDMS membrane is strategically placed between the microchannel and the substrate. This design eliminates direct contact between the fluid and the electrodes, minimizing particle and cell exposure to any residual fringing electric fields.(33) The PDMS insulating properties and dielectric behavior effectively suppress such fields, and the membrane structure provides additional practical advantages: it enables easy replacement of the microfluidic channel while reusing the same substrate, facilitating repeated experiments with consistent acoustic performance.(34, 35) Although minimal residual electric fields may still penetrate, their influence is negligible compared to the acoustic effects, as investigated by Collins et al.,(36) who reported that the TSAW-induced ARF dominates over the accompanying electric forces by several orders of magnitude. This ensures that the observed particle behavior is primarily governed by the acoustic interactions.



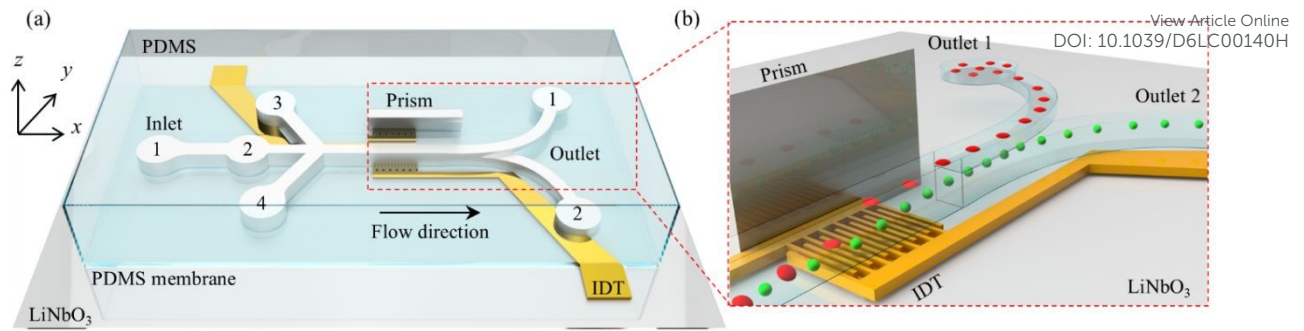


Fig. 1. (a) Schematic diagram of the vertical-type acoustofluidic device, (b) Focused image showing a micro-prism for side-view visualization and a downstream vertical bifurcation diverging horizontally into two separate outlets.

2.2 Numerical investigation of asymmetric wave scattering from oblate spheroids with varying orientation and aspect ratio

Our hypothesis for the proposed shape-based separation of oblate spheroids from spheres in the proposed vertical-type acoustofluidic device is that (i) the rotational motion of the oblate spheroids is suppressed by the counter-rotating TSAW-induced ART, leading to horizontal alignment with their minor (shorter) axis (2b) parallel to vertical wave propagation (+z-direction) (Fig. 2a), and (ii) the increased projected area of the horizontally aligned oblate spheroids, perpendicular in the xy -plane in Fig. 1(a), results in an increase in the ARF magnitude, leading to further vertical migration compared to the spheres. For validation, we conducted numerical simulations for the wave scattering from oblate spheroids with varying AR as in Fig. 2. In the numerical calculation, we modeled a spherical PS particle with a diameter of $5\ \mu\text{m}$ and its isovolumetric oblate particles with varying orientation and AR. Incident plane progressive waves are propagating in the +z-direction (from 270° to 90°) with a frequency of 141 MHz to have κ of 1.5 for effective PS particle manipulation by the ARF (ARF factor as a function of κ can be found in Fig. S1).⁽³⁷⁾ Fig. 2a demonstrates our numerical simulation model for acoustic wave scattering from oblate spheroids with varying orientation and AR, defined as the ratio of minor axis (2b) divided by major axis (2a). To isolate the primary vertical component of the leaky LWs, we modeled a +z-propagating plane wave and neglected lateral LW components ($\pm x$ -direction) due to their minimal contribution to vertical migration. The oblate spheroid was placed within a computational domain of radius R_i , surrounded by a perfectly matched layer (PML) (For further details of numerical simulation, see supplementary information).

In our numerical approach, we simplified the phenomenon to focus on the dominant physical mechanisms, namely, the asymmetric wave scattering from oblate spheroids with varying orientation and AR. First, we modeled the fluid as inviscid, thereby neglecting the acoustic streaming effect, induced by wave attenuation due to viscous damping. While acoustic



streaming may be present, its influence on shape-based separation is minimal, as will be explained later with experimental validation (in Section 2.7), because the particle size and wavelength under the operating conditions yield Helmholtz number comparable to 1 (Mie scattering regime) where radiation dominates streaming effects.(38) Second, the assumption of rigid particles provides first-order approximation that captures the essential behavior of shape-induced responses without the added complexity due to deformation. While biological particles like RBCs are indeed deformable, the dominant acoustic interactions, especially at moderate power levels, are primarily governed by geometry rather than minor morphological deformation. Third, the single-particle model neglects the particle-to-particle interactions effect such as secondary ARF. This is a reasonable approximation given the dilute sample conditions used in our experiments to minimize the inter-particle effects. However, we acknowledge that in high-concentration samples (e.g., clinical RBC assays), these effects may become significant and should be addressed in future work. Overall, these assumptions are deliberate, enabling focused investigation of shape-specific ARF and ART without introducing insignificant confounding effects from viscous or collective dynamics.(39)

Fig. 2b shows a polar scattering plot for an oblate spheroid with AR of 0.45 at varying orientation (θ) at a distance of $R_{ext} = 100 \mu\text{m}$. The wave scattering can be classified into forward (90°), backward (270°), and side scattering (0° and 180°).(30, 40) The asymmetry in the side scattering generates an ART on the particle (ART formula available in supplementary information).(41-43) The oblate spheroids exhibit distinct rotational motions, including tumbling, kayaking, and log-rolling. These arise from the velocity gradient in a Poiseuille flow.(44) For $\theta = 0^\circ$ (black), the two components of the side scattering were balanced, and no net torque was induced for the spheroid. On the other hand, for $\theta = 30^\circ$ (red), 45° (blue), and 60° (magenta), the asymmetric side scattering was observed, and the imbalance in the side scattering increased with increasing orientation. These results indicate that the TSAW-induced counter-rotating ART suppresses the rotational motion of the oblate spheroids. As a result, the particles align horizontally with the major axes (2a) aligned with the xy -plane to have $\theta = 0^\circ$ in Fig. 2a. This alignment increases the projected surface area perpendicular to the wave propagation, resulting in the enhanced ARF, which is proportional to the projected surface area, exerted on the oblate objects.

A polar scattering plot for oblate spheroids with varying AR is shown in Fig. 2c. With reference to the sphere with AR = 1.00 (black), the isovolumetric oblate spheroids with AR = 0.45 (red), 0.25 (blue) and 0.18 (magenta) exhibited increasing backward scattering (270°) that is proportional to the ARF magnitude.(40) These results indicate that the magnitude of the ARF



increases as the particle morphology changes from spherical ($AR = 1$) to oblate (smaller AR) and that the horizontally aligned oblate spheroids experience more significant ARF than the isovolumetric spheres. Further details on ARF and ART in terms of wave scattering can be found in supplementary information. As the oblate objects experience a larger magnitude of the ARF compared to the spherical objects with the same volume, we can infer that the oblate spheroids would show further vertical migration than the spheres in the proposed vertical-type acoustofluidic device. This difference in the vertical trajectories of two different shaped isovolumetric micro-objects allows separation at a downstream vertical bifurcation connected to separate outlets (Fig. 1b).

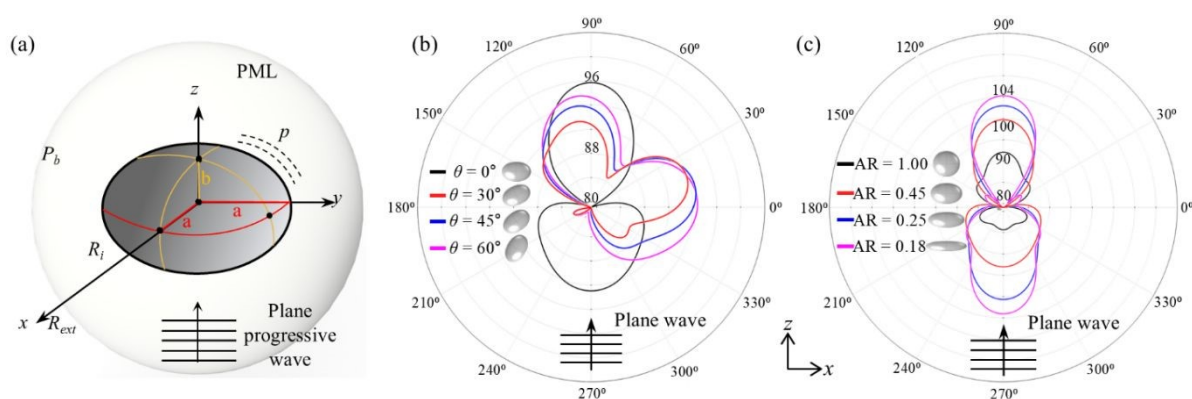
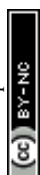


Fig. 2. (a) An oblate spheroid exposed to incident plane progressive waves. Polar scattering plots for oblate spheroids (b) with varying orientation (θ) of 0° , 30° , 45° , and 60° and (b) with varying aspect ratio (AR) of $= 1.00$, 0.45 , 0.25 and 0.18 .

2.3 Fabrication of spherical and oblate PS microparticles

For experimental validation of the proposed acoustofluidic approach for the shape-based separation, we first fabricated PS microspheres and transformed them into oblate spheroids with varying AR by film-squeezing. The monodisperse PS spherical microparticles were synthesized by dispersion polymerization,^(45, 46) and the derivate oblate PS microparticles were fabricated by film-squeezing the spherical microparticles.⁽⁴⁷⁾ Further details can be found in Experimental. Fig. 3a–f presents the SEM images of all the fabricated PS particles used in our experiments. The monodispersity of the PS microspheres with a diameter of 5 and $1.2 \mu\text{m}$ (Fig. 3a and e) was confirmed in the size distribution analysis in Fig. 3g. In the film squeezing process for the morphology transition from spherical to oblate, we varied the film squeezing pressure to fabricate the oblate spheroids with varying AR of 0.45 , 0.25 , and 0.18 from the $5 \mu\text{m}$ PS spherical particles and with an AR of 0.18 from the $1.2 \mu\text{m}$ spherical particles, as shown in Fig. 3b, c, d, and f, respectively. Although the oblate spheroids were found to be slightly polydisperse, compared to the original microspheres, we found that the three kinds of the oblate spheroids had distinct size distributions (Fig. 3g).



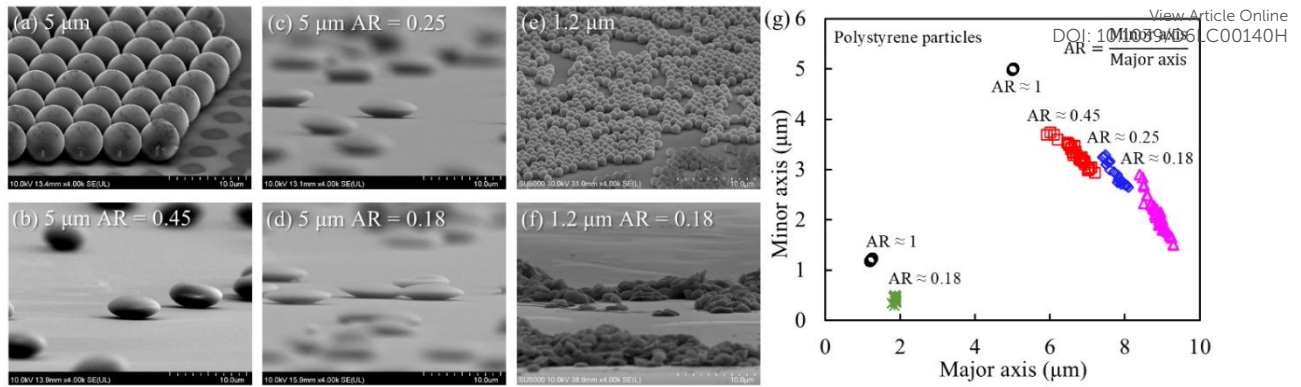
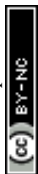


Fig. 3. SEM images of the 5 and 1.2 μm -diameter PS particles used in the experiments. (a and e) original microspheres, and oblate spheroids with AR of (b) 0.45, (c) 0.25, (d) 0.18, (f) 0.18 and (g) size distribution of the particles.

2.4 Horizontal alignment of oblate spheroid by acoustic radiation torque

For experimental validation of the horizontal alignment of the oblate spheroids, we examined the orientation of sphere and oblate spheroids before and after the interaction with the TSAW field (Fig. 4 and Supplementary Movie 1). The spheres might rotate in a Poiseuille flow, but their rotational motion cannot be observed due to the geometric symmetry in Fig. 4a and b. Both before and after interaction with the acoustic field, the spheres remained at the same focal. In contrast, the oblate spheroids displayed random orientations and rotational dynamics, mainly kayaking and tumbling, before encountering the acoustic field (Fig. 4c).⁽⁴⁴⁾ These freely rotating oblate particles experienced asymmetric side scattering when exposed to the traveling acoustic field, the rotational motion of the oblate spheroids was suppressed by the ART, resulting in horizontal alignment with their minor axis (2b in Fig. 2a) parallel to the vertical propagation of the leaky LWs (+z-direction), as shown in Fig. 4d. The inset images in Fig. 4d further confirm the horizontal alignment after the oblate spheroids passed through the acoustic field (see also Supplementary Movie 1, corresponding to Fig. 4). The rotational dynamics of oblate particles in acoustic fields have been previously investigated. Hoque et al. reported that oblate particles experience acoustic radiation torque in standing wave fields, which governs their orientation and rotational behavior.⁽⁴⁸⁾ These findings are consistent with our observations, where ART suppresses rotational motion and induces stable horizontal alignment under TSAW excitation. The ART-induced horizontal alignment with major axes (2a in Fig. 2a) in the xy -plane increased the projected surface area normal to the wave propagation, thereby amplifying the net vertical ARF experienced by the oblate objects. As a result, unlike the spheres in Fig. 4a and 4b, the oblate spheroids exhibited a greater vertical migration distance; this increased vertical migration can be substantiated in Fig. 4d, where the oblate spheroids were captured at a higher focal plane approximately 600 μm above the IDT, compared to their



pre-alignment position in Fig. 4c. It should be noted that, although both horizontal and vertical components of the acoustic wave are generated due to leakage at the Rayleigh angle ($\sim 22^\circ$), the vertical component becomes dominant in the present configuration. This is because the surface acoustic wave propagating along the substrate continuously leaks energy into the fluid at an oblique angle, resulting in a significant transfer of momentum in the vertical direction. Additionally, the confinement of the microchannel and the interaction of the leaky wave with the fluid–solid interface enhance upward acoustic radiation effects. As a result, the effective vertical component of the acoustic radiation force is significantly greater (approximately 2.5 times) than the horizontal component, making it the dominant factor governing particle trajectories in this vertical-type acoustofluidic platform. (49, 50)

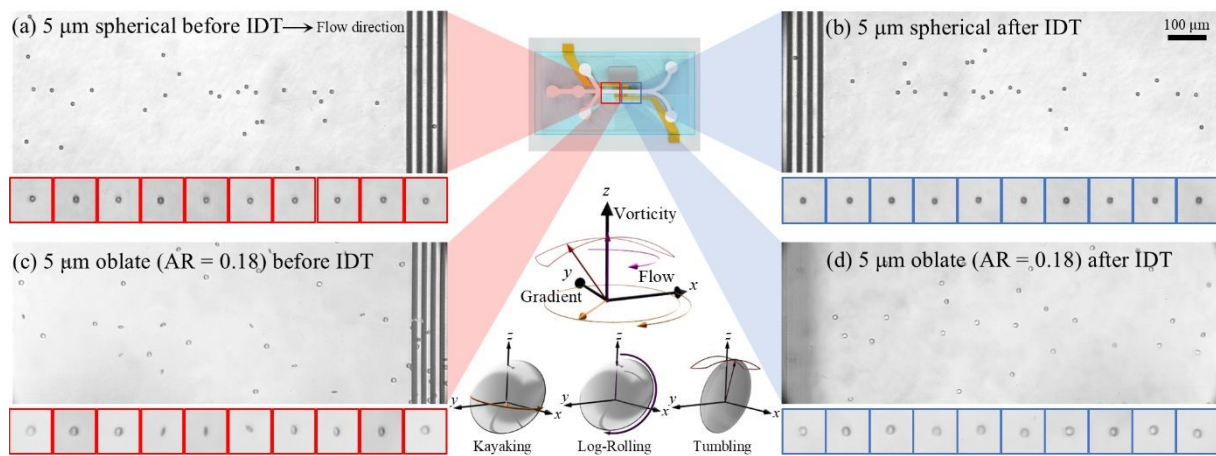


Fig. 4. Microscopic snapshot images of acoustofluidic vertical alignment of (a & b) spherical and (c & d) oblate microparticles.

2.5 Investigation of vertical migration using micro-prism: side-view visualization

The proposed acoustofluidic approach for the shape-based separation of oblate spheroids from spheres is based on varying vertical trajectory depending on the oblate spheroid AR. As the vertical migration of the particles is difficult to observe in the conventional microscopy, we introduced a micro-prism alongside the microchannel for the side-view visualization of the particles, as shown in Fig. 5a. With the side illumination, the scattered fluorescence light can be detected in the microscopy through the mirror side of the prism. (32) As investigated earlier, the oblate particles are horizontally aligned by the ART and migrate vertically by the ARF (Fig. 5b) while the spherical particles only experience the ARF with its magnitude less than that exerted on the oblate ones (Fig. 5c) in the acoustic field. Fig. 5d summarizes the experimental results of the vertical displacement (d_V) as a function of the electrical power (P_e) applied to the IDT for spherical (black) and oblate particles with AR = 0.45 (red), 0.25 (blue), and 0.18 (magenta). Overall, with increasing P_e , the d_V value was measured to increase accordingly due to the increasing ARF magnitude proportional to P_e for all kinds of the particles. As the particle



shape changed from spherical to more oblate (smaller AR), the d_V value increased at the fixed P_e conditions because the ARF magnitude was enhanced by the increased projected area due to the horizontal alignment of the oblate particles caused by the ART.

Fig. 5e–h presents the microscopic side-view images obtained through the prism, showing varying vertical migration of the particles depending on P_e and AR of the PS microparticles. The microchannel had a height of 700 μm with a downstream vertical bifurcation located 500 μm above the microchannel bottom. We confirmed that the side-view visualization of the fluorescent PS microparticles with varying AR can be achieved in our micro-prism-embedded microchannel. From the experimental results, by applying frequency of 141 MHz we found that the lower P_e required for the particles to reach the same d_V tended to decrease with decreasing AR (more oblate). In other words, at the same P_e , the d_V increased with decreasing AR. For example, at $P_e = 30$ mW, the d_V value was measured to be approximately 645, 510, 470, and 390 μm for AR = 0.18 (magenta), 0.25 (blue), 0.45 (red), and 1.00 (black) respectively. With the vertical bifurcation located 500 μm above the microchannel bottom, the oblate particles with AR = 0.18 and 0.25 with d_V greater than 500 μm can be collected in the upper outlet (Outlet 1) while the spherical and oblate particles with AR = 0.45 with d_V smaller than 500 μm can be collected in the lower outlet (Outlet 2), as will be demonstrated later.

Importantly, it should be noted that what enables the proposed shape-based separation is not the absolute value of the vertical migration distance (d_V) but the relative migration difference (Δd_V) between the particle types. In our previous cross-type acoustofluidic platform,⁽³⁰⁾ we observed that the ART suppressed the rotation of prolate spheroids, thereby minimizing their projected area perpendicular to the wave propagation and reducing the ARF magnitude in comparison to the isovolumetric spheres. This enabled label-free separation between spherical and prolate particles, though the difference in lateral migration was limited to approximately 50 μm . In contrast, the proposed vertical configuration aligns the oblate spheroids such that their major axes align perpendicular to the vertical wave propagation, enhancing the interaction mainly with the vertical component of the travelling wave field, which is 2.5 times more significant than the horizontal counterpart due to the Rayleigh angle of 22° at LiNbO₃/water interface. As a consequence, we achieved the vertical migration difference exceeding 100 μm , significantly enhancing separation efficiency and stability (Fig. 5). This enhanced migration not only improves the purity and robustness of particle separation but also offers valuable design insights. In the cross-type acoustofluidic platform, the projected surface area, normal to the horizontal ARF component, remains relatively unchanged between the oblate spheroids and spheres; therefore, these two shapes cannot be effectively distinguished or separated. However,



transitioning from the cross-type to vertical-type configurations addresses this limitation of the previous device, enabling the effective separation of oblate spheroids from spheres, which has remained as an unmet need despite importance and necessity.

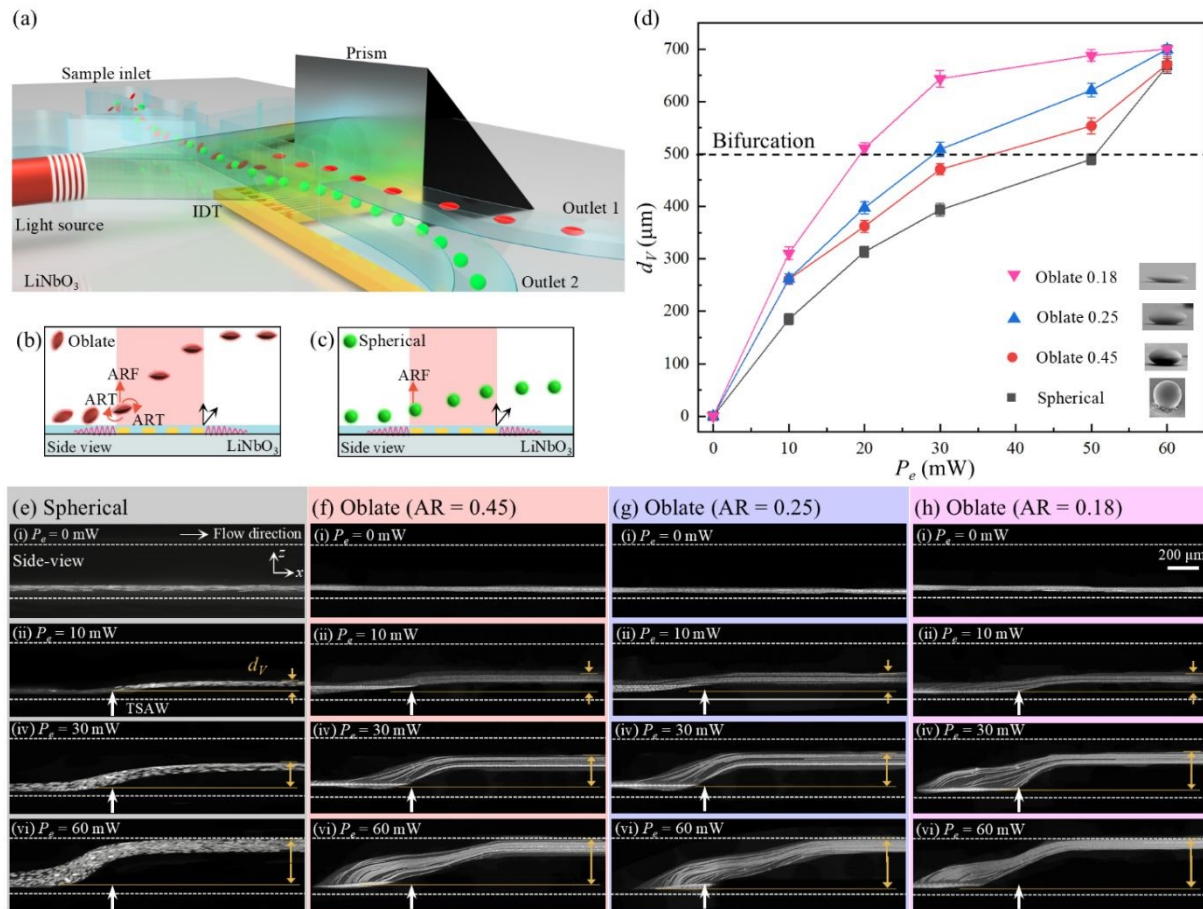


Fig. 5. a) A schematic diagram of the proposed acoustofluidic device with a micro-prism for side-view visualization. Side-view at midstream microchannel for b) oblate and c) spherical particles. d) vertical displacement (d_v) of the particles with varying AR and electrical power (P_e) applied to the IDT. e–h) microscopic prism-view of the different particles.

2.6 Investigation of particle trajectories in a vertical bifurcation microchannel: bottom-view visualization

Fig. 6a–c illustrate the various particle trajectories depending on the particle shape at the downstream vertical bifurcation, connected to upper and lower outlets (Outlets 1 and 2, respectively) for separate collection. In Fig. 5, the vertical displacement by the ARF was measured to be $d_v \cong 190, 260, 260,$ and 310 μm at $P_e = 10$ mW, $395, 470, 510,$ and 643 μm at $P_e = 30$ mW, $660, 665, 690,$ and 700 μm at $P_e = 60$ mW for the spherical and oblate particles with AR = 1.00 (black), 0.45 (red), 0.25 (blue), and 0.18 (magenta), respectively. The downstream vertical bifurcation was installed at a height of 500 μm inside the microchannel and diverged horizontally into two separate outlets to allow the bottom-view visualization under an inverted microscope. After the bifurcation, the vertically upper channel was connected to the



horizontally upper outlet (Outlet 1) while the vertically lower channel was linked to the horizontally lower outlet (Outlet 2). In the bottom-view visualization (without micro-prism), the varying horizontal trajectory after the vertical bifurcation toward either outlet was observed in Fig. 6d, f, h, and j depending on the particle AR and wave amplitude (P_e applied to the IDT). Without the acoustic field, all the particles were flowing toward the lower outlet after the vertical bifurcation. The collected particle fractions from the two outlets as a function of P_e are shown in Fig. 6e, g, i, and k (black for upper Outlet 1 and red for lower Outlet 2); supplementary Fig. S2 presents fluorescent microscopy images of the green-fluorescent spherical and red-fluorescent oblate PS microparticles collected at Outlet 1 and Outlet 2. At $P_e = 10$ mW, the vertical migration for all the particles was smaller than the vertical bifurcation height, and all the particles were flowing through the lower outlet. On the other hand, at $P_e = 30$ mW, both oblate spheroids with AR = 0.25 and 0.18 showed the vertical migration greater than the vertical bifurcation and thus passed through the upper outlet (Outlet 1) unlike the spherical and oblate particles with AR 0.45. With further increased P_e of 60 mW, all the particles experienced the ARF with a sufficient magnitude to reach the microchannel ceiling and consequently migrated toward the upper outlet. These results suggest that the proposed acoustofluidic platform can be applicable to the shape-based separation of oblate spheroids from spheres depending on the particle shape under the same acoustic field at a fixed P_e condition.

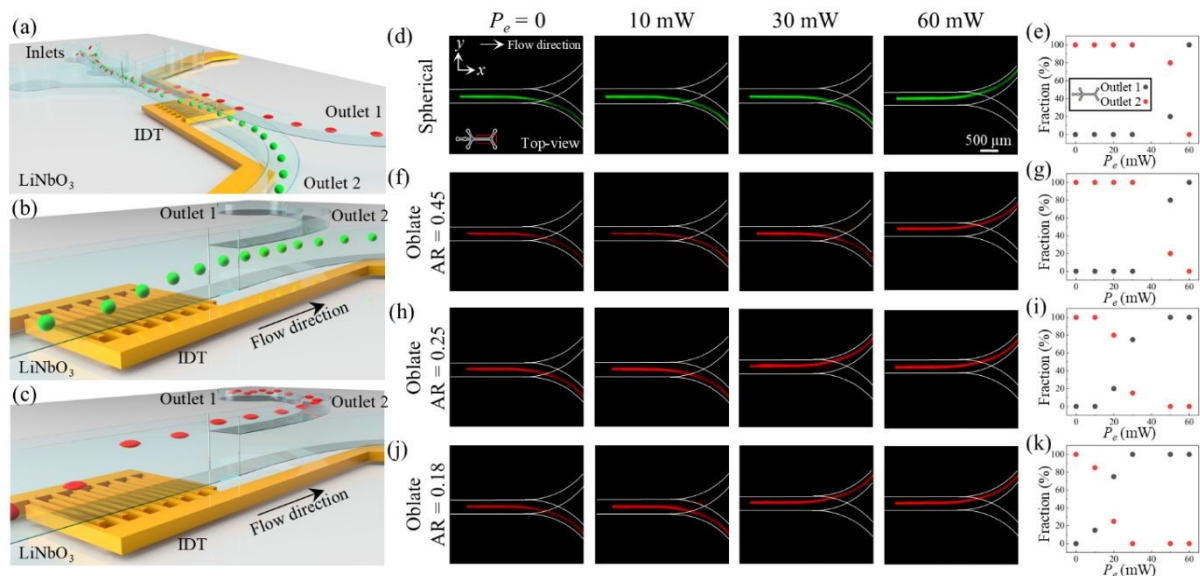
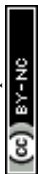


Fig. 6. a–c) Illustrations of the trajectories of spherical and oblate particles in a vertical bifurcation microchannel; d, f, h, and j) Bottom-view visualization of the spherical and oblate PS microparticles with different AR and P_e at the bifurcation. Panels e, g, i, and k show the particle distribution across the two outlets as a function of P_e .

2.7 Acoustofluidic shape-based separation of oblate spheroid from sphere



In the proposed acoustofluidic device with a vertical configuration, we hypothesized that the acoustic streaming effect was negligible to the demonstrated shape-based separation even in a relatively high channel (height of 700 μm) under high-frequency excitation at 141 MHz. This is attributed to our earlier claims that (i) it is not the vertical migration itself but the difference in the vertical migration that enables the proposed shape-based separation in the vertical-type acoustofluidic platform and that (ii) the frequency for separation was carefully chosen such that the scatter size (particles or cells) was comparable to the acoustic wavelength to induce the asymmetric Mie scattering for the ART and ARF acting on the scatter. For validation of our hypothesis, we conducted a negative-control experiment using the isovolumetric spherical ($\sim 1.2 \mu\text{m}$) and oblate (AR of 0.25) particles (green- and red fluorescent in Fig. 7, respectively) with low Helmholtz number. In this Rayleigh scattering regime, as the influence of the acoustic streaming dominated over the acoustic radiation, we could assume that the effects of the TSAW-induced ART and ARF were negligible. In other words, the vertical migration of the particles was solely attributed to the streaming-induced hydrodynamic force. As shown in Fig. 7, we found that both particles were flowing through the lower outlet regardless of the application of the acoustic field. It indicates that the shape-based separation cannot be achieved by the acoustic streaming effect. The acoustic streaming-induced hydrodynamic drag force might cause the vertical migration to some extent; however, it was equal for the particles of both shapes with no noticeable difference in the trajectories even under the elevated P_e condition up to 1.6 W (Fig. 7b), far exceeding the operational level (30 mW) for the radiation-based sorting (Fig. 6). From the observations, we can conclude that the main working principle of the proposed shape-based method is the combined effects of acoustic radiation and torque, not streaming.

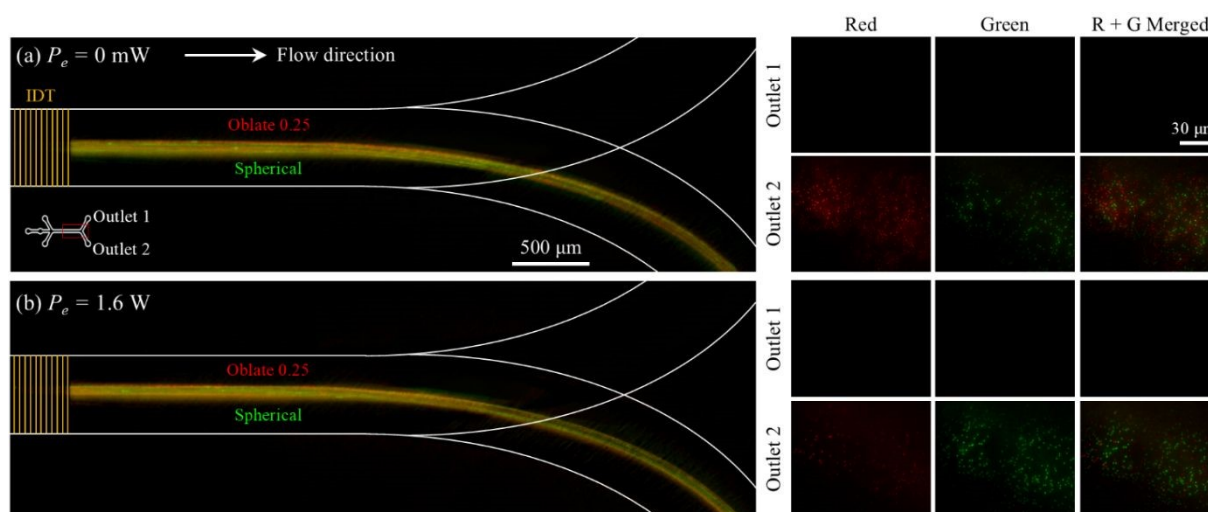


Fig. 7. Acoustofluidic shape-based separation of low Helmholtz number-particles ($\sim 1 \mu\text{m}$) of oblate and spherical shapes (a) without P_e and (b) with P_e .



Building on the numerical and experimental findings, we successfully demonstrated the shape-based separation of the oblate spheroids from the spherical particles in the proposed device in Fig. 8. For clear distinction in the fluorescent images and quantitative analysis of the separation efficiency, we used the red- and green-fluorescent PS microparticles with varying AR; however, this fluorescent labeling is simply for better visualization, not a prerequisite of the proposed label-free acoustofluidic shape-based separation. Fig. 8a demonstrates the acoustofluidic shape-based separation of the red-fluorescent oblate (AR = 0.18) and green-fluorescent spherical PS microparticles at $P_e = 30$ mW. The red oblate particles horizontally aligned by the ART in the acoustic field and experienced greater ARF than the green spherical particles. All the red oblate particles were collected at upper Outlet 1 while all the green spherical particles were retrieved at lower Outlet 2 with 100% purity and recovery rate (Fig. 8d). In Fig. 8b, even with smaller AR difference, the similar results were obtained for the two distinct-shaped particles (red oblate with AR = 0.25 and green spherical) at $P_e = 30$ mW. A reduction in the AR difference led to a slight decrease in the purity of 100% and 92.5% and recovery rate of 96% and 100% for oblate (AR = 0.25) and spherical particles, respectively (Fig. 8e). The proposed acoustofluidic shape-based separation method was found to be applicable to not only between the spherical and oblate particles, but also between the oblate spheroids with different ARs. Fig. 8c shows that the red-fluorescent oblate particles with AR = 0.18 can be separated from the green-fluorescent oblate particles with AR = 0.45 at $P_e = 30$ mW. Both oblate spheroids were horizontally aligned by the ART in the acoustic field. As in our numerical simulation results in Fig. 2c, the more oblate-shaped spheroids (red, AR = 0.18) experienced the greater magnitude of the ARF than less oblate-shaped spheroids (green, AR = 0.45) due to the greater acoustic backward scattering caused by the larger projected surface area. All the red oblate with AR = 0.18 particles were collected at upper Outlet 1 while all the green oblate with AR = 0.48 particles were retrieved at lower Outlet 2 with 100% purity and recovery rate (Fig. 8f). All the results in Fig. 8 were in good agreement in the sorting experiments in Fig. 5 and 6.

View Article Online
DOI: 10.1039/D6LC00140H



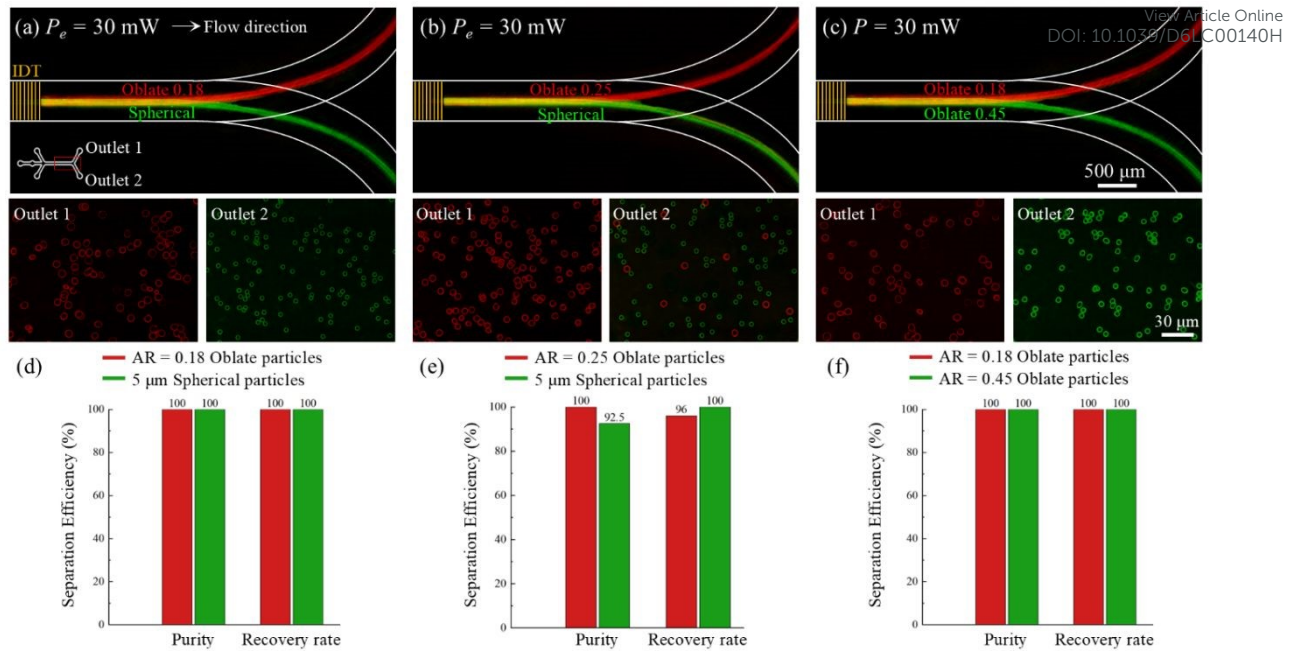


Fig. 8. Acoustofluidic shape-based separation of (a) oblate with $AR = 0.18$ and spherical, (b) oblate with $AR = 0.25$ and spherical, and (c) oblate with $AR = 0.18$ and 0.45 . d–f) Purity and recovery rate analysis for the collected particles after separation.

2.8 Acoustofluidic shape-based separation of oblate and spherical RBCs

For validation of the practical applicability, we applied the proposed acoustofluidic approach for separation of oblate and spherical RBCs, as shown in Fig. 9. We modified the normal oblate RBC morphology into the sphere based on osmolarity-dependent shape transition. We used a NaCl solution of 189 mOsm/kg H_2O to achieve the spherical-shaped RBCs without compromising their integrity.⁽⁵¹⁾ We first conducted the RBC sorting experiments separately for the spherical and oblate RBCs, in which the latter samples required the osmolarity-induced RBC shape change. Fig. 9a illustrates the acoustofluidic shape-based RBC separation in the proposed device. The SEM images confirmed the biconcave RBC shape without any treatment (Fig. 9b) and the osmolarity-induced spherical-like RBCs (Fig. 9c), in which the RBC volume remained almost the same. We conducted the RBC sorting experiments with a frequency of 65 MHz tailored to the RBC properties (details can be found in Fig. S2). Fig. 9d shows the varying trajectory of the morphology-altered spherical RBCs at the vertical bifurcation depending on P_e applied to the IDT. Due to the spherical shape, the abnormal RBCs experienced comparably less ARF and thus flowed toward the lower outlet until $P_e = 50$ mW. With the increased P_e of 70 mW, the spherical RBCs vertically migrated further than 500 μm and thus were collected at the upper Outlet 1. On the other hand, the biconcave normal RBCs in Fig. 9e experienced the TSAW-induced ART due to the asymmetric side scattering, leading to the horizontal RBC



alignment. The increased projected surface area caused the ARF acting on them to increase so that their vertical migration was greater than that of the spherical RBCs at the same acoustic intensity conditions. The vertical trajectory transition of the normal RBCs was observed at $P_e = 30$ mW, lower than the threshold power required for the spherical RBCs ($P_e = 70$ mW in Fig. 9d).

Following the sorting experiments, we conducted the simultaneous separation experiments using mixed populations of spherical and oblate, disc-shaped RBCs, as shown in Fig. 9f. Until low P_e applied to the transducer up to 20 mW, neither spherical nor oblate RBCs experienced sufficient ARF to have a vertical migration exceeding 500 μm (location of the vertical bifurcation at downstream). Both-shaped RBCs were collected from the lower outlet (Outlet 2), as can be expected from the independent sorting experiment results. Upon increasing the power up to 30 mW, significant ARF was exerted on the horizontally oriented oblate RBCs, leading to their trajectories translocated to the upper outlet (Outlet 1), separated from the spherical RBCs. At $P_e = 50$ mW, even a few non-target spherical RBCs exhibited sufficient vertical migration and passed through the upper outlet, together with the oblate RBCs. At $P_e = 70$ mW, both oblate and spherical RBCs experienced significant ARF and thus vertically migrated into the upper Outlet 1.

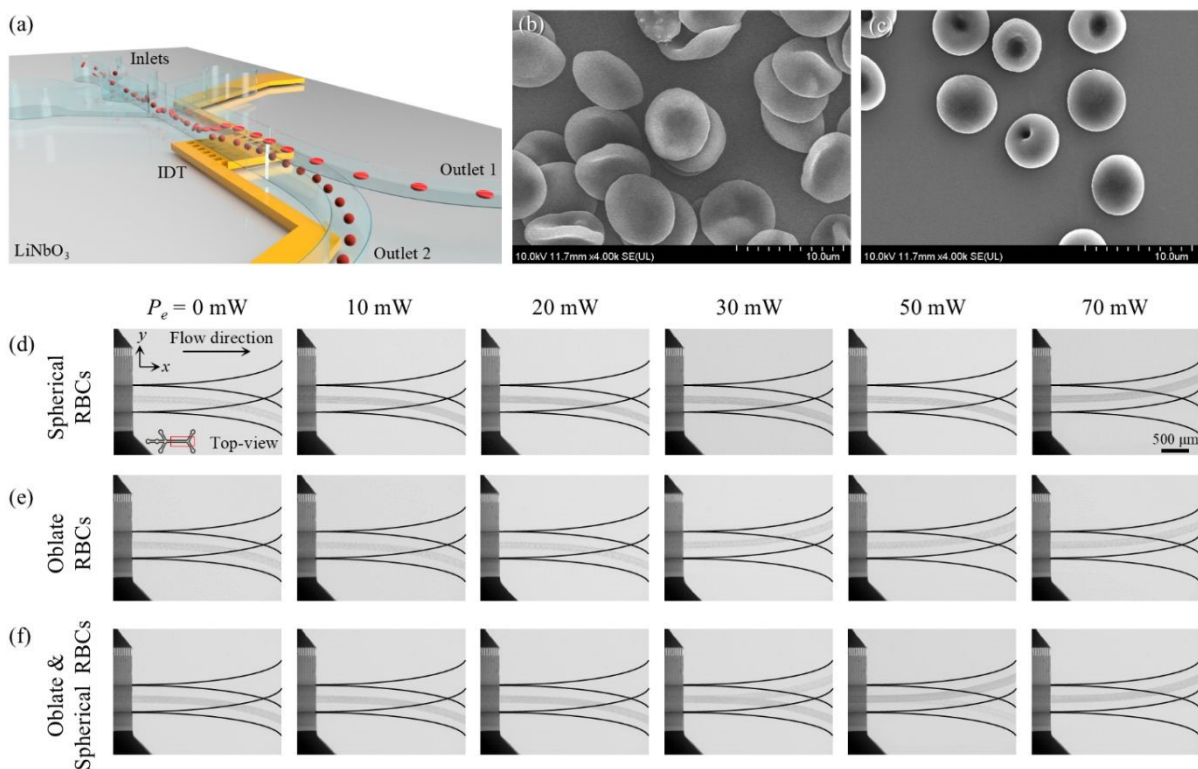


Fig. 9. a) Schematic of vertical-type acoustofluidic device for the shape-based RBCs sorting. Scanning electron micrographs of b) normal biconcave-shaped RBCs prior to osmotic treatment, and (c) RBCs in hypotonic solution (189 mOsm/kg H₂O). RBC sorting images for (d) spherical-shaped and (e) biconcave-shaped RBCs at varying P_e .



For quantitative evaluation of the shape-based RBC separation efficiency, we utilized the fluorescence-labeled RBCs (oblate in green and spherical in red) even though the proposed acoustofluidic approach does not require any label for separation. The labeling did not affect cell morphology or behavior but enabled fluorescence-based analysis of the RBCs with two different shapes. Fig. 10 shows the purity of the collected abnormal spherical and normal oblate RBCs at both outlets at varying P_e applied to the transducer. For quantification, we calculated the purity by assuming the oblate and spherical RBCs as the targets for the upper and lower outlets, respectively. From P_e of 0 to 20 mW, the purity of the abnormal RBCs was 50% as both-shaped RBCs were all collected in the lower outlet (Fig. 10a–c). At $P_e = 30$ mW, the purity of the normal RBCs with green fluorescence at Outlet 1 was 100% while that of the abnormal RBCs with red fluorescence at Outlet 2 was 86%, indicating a few oblate RBCs remained with the spherical RBCs (Fig. 10d). This impurity may be attributed to the non-uniformity of the normal RBCs in size and shape, as in Fig. 9b. With the elevated power of 50 mW, on the other hand, the purity of the abnormal, spherical RBCs increased to 100% while that of the normal, oblate RBCs reduced to 90% since a few spherical RBCs vertically migrated to the upper outlet (Fig. 10e) due to the polydispersity in shape and size, as in Fig. 9c. At $P_e = 70$ mW, the purity of the normal RBCs was 50% as all the RBCs were collected in upper outlet (Fig. 10f). These results underscore the importance of the optimization of the operating conditions, especially P_e , for efficient acoustofluidic shape-based separation. It should be highlighted that the proposed acoustofluidic device in the vertical configuration enables the first demonstration of the RBC separation based on the cell morphology in a label-free manner.

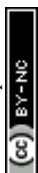
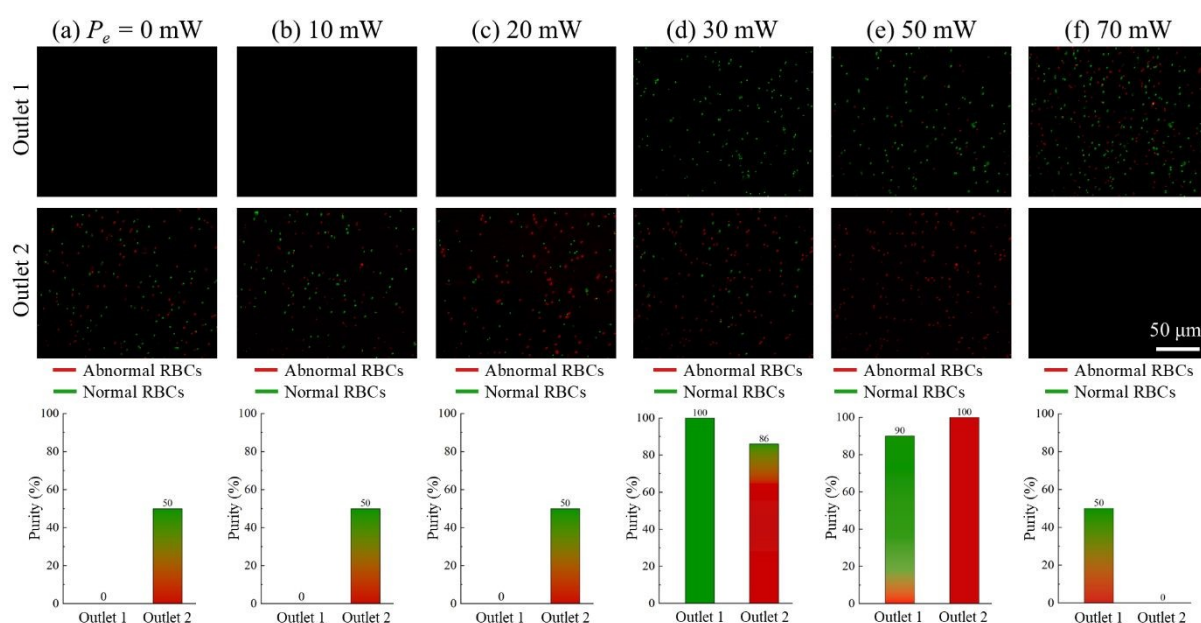


Fig. 10. (a–f) Quantitative evaluation of the shape-based RBC separation by collected samples at the outlets at different P_e with their purity at each outlet. Article Online
DOI: 10.1039/D6LC00140H

It is worth noting that, the magnitude of ARF exerted on an object is proportional to the wave amplitude squared and also electrical power applied to the transducer,(52) regardless of acoustic frequency. In our experiments, we used the 5 μm spherical PS particles and their derivative isovolumetric oblate particles with varying aspect ratio whereas the normal oblate RBC size ranged from 6 to 8 μm under healthy conditions. The non-uniform size distribution of the oblate particles (Fig. 3g) and RBCs (Fig. 9b and 9c) might have reduced the separation efficiency in the experimental demonstrations. Moreover, in Fig. 8, the separation of isovolumetric oblate and spherical PS particles were achieved at P_e of 30 mW. On the contrary, in Fig. 10, we applied comparable or larger P_e for separation of the oblate and spherical RBCs although the RBC size was larger than the PS particles. This can be attributed to the reduced difference in acoustic impedance contrast for the RBCs compared to the PS microparticles. As the acoustic impedance contrast at the RBC/water interface was smaller than that at the PS particle/water, the higher electrical power would have been applied for the shape-based RBC separation.

It is important to note that healthy RBCs typically exhibit a relatively uniform biconcave (discocyte) morphology with limited variation in aspect ratio under physiological conditions. In contrast, under pathological conditions such as hereditary spherocytosis, RBCs transform from biconcave discocytes into near-spherical spherocytes due to membrane loss and structural alterations, resulting in a significant reduction in shape anisotropy.(53) In this study, spherical particles are used as representative models for such abnormal RBC morphologies. Therefore, the proposed method is particularly suited for separating particles with pronounced shape differences, while separation of subtle variations within healthy RBC populations is beyond the scope of the present work.

3. Conclusions

We developed an acoustofluidic platform in the vertical configuration for shape-based separation of the oblate spheroids from spheres in a label free manner based on the TASW-induced ART and ARF. Our numerical and experimental investigations revealed that asymmetric side scattering exerts a counterrotating ART on the oblate particles, repressing the rotation of the oblate objects and thus aligning their shorter, minor axis parallel to the wave propagation. This horizontal alignment increases the projected surface area of the oblate spheroids to the vertical wave propagation, enhancing backward scattering and amplifying the ARF. The increased ARF acting on the oblate micro-objects allows them to have further vertical



migration than the isovolumetric spherical ones. Based on these findings, we successfully demonstrated the shape-based separation of the spherical and oblate PS microparticles and RBCs at high purity and recovery rate.

4. Experimental

Microfluidic Device

The IDT composed of a bimetallic layer of Cr and Au (thickness of 20 and 100 nm, respectively) were deposited on a 500 μm -thick 128°-rotated, Y-cut, X-propagating LiNbO₃ substrate (MTI Korea) by means of the photolithography, E-beam evaporation, and lift-off procedure.⁽⁵⁴⁾ Two set of IDTs were utilized in the experiments, one having comb-shaped electrode spacing ($\lambda/4$) of 7 μm and other with a comb-shaped electrode spacing ($\lambda/4$) of 15.2 μm with a total aperture of 1 mm and consists of 30 electrode pairs. A vector network analyzer (E5071B, Agilent Technologies) was used to determine the resonant frequency of the straight IDTs as 141 MHz and 65 MHz respectively. A Fig. S3 shows the S_{11} measurement data of both IDTs by a vector network analyzer. For applications of RF AC signals to the straight IDT, an RF signal generator (BSG F10, Belektronig GmbH) was used. To fabricate the bifurcated rectangular PDMS microchannel, the 3D mold was created with 3D printer and then the soft lithography process was performed to create 3D microchannel. The mold was pre-treated with 1H, 1H, 2H, and 2H-Perfluorooctyltriethoxysilane (Sigma-Aldrich) before pouring the PDMS mixture (Sylgard 184A and 184B, Dow Corning) on it. The rectangular microchannel had a height (h) of 700 μm and a width (w) of 300 μm . The micro-prism of 2 mm \times 2 mm (N-BK7 Right Angle Prism, Edmund Optics Worldwide) was placed on the side of the microchannel 2 mm away from the microchannel wall. After fabricating the prism-embedded microchannel, the microchannel chip was bonded to the substrate using oxygen plasma treatment (Covance, Femto Science). Fluorescent PS microspheres with a diameter of 5 μm were sourced from (Thermo Scientific, Inc.). The sample and sheath fluid were injected into the microchannel using a syringe pump (neMESYS Cetoni GmbH), with particles suspended in distilled water (Dyne Bio Inc). For observe the behavior of the particles, we used a high-speed CMOS camera (VEO 710L, Phantom) paired with an inverted microscope (IX73, Olympus).

Microparticle Fabrication

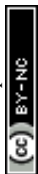
Fabricating PS spherical microparticles with a diameter of 5 μm , 1.6 g of polyvinylpyrrolidone (PVP, Sigma-Aldrich) was first dissolved in 210 g of butanol and magnetically stirred for 1 h. The butanol solution containing PVP was added to a 40 g solution of styrene monomer



containing 0.4 g of azobisisobutyronitrile (AIBN) in a 500 ml three-necked double-jacket reactor equipped with a reflux condenser, and then polymerization was initiated. The polymerization was performed at 70°C and 120 rpm for 24 h under N₂ atmosphere. Generating oblate microparticles, polyvinyl alcohol (PVA) (Sigma-Aldrich) was used to prepare a polymer film containing monodisperse PS spherical microparticles for uniaxial squeezing. First, 7.5 g of PVA was added to 150 ml of distilled water at 80°C and sufficiently dissolved using magnetic stirring for 4-5 h. 0.1 wt% of PS spherical microparticles were added to this PVA aqueous solution. The uniformly dispersed mixture was poured onto a flat aluminum tray and dried to obtain a flexible PVA film containing PS spherical microparticles. Fabrication of oblate microparticles, the film was cut into a circular shape and was placed between two silicone rubber sheets (HSW Co., South Korea) to form a three-layered composite. The composite consisting of these three layers was uniaxially squeezed using a press at 135°C with a compression range of 17–83%. The squeezed film with different degrees of compression were dissolved in distilled water at 80°C and then centrifuged to recover the PS oblate microparticles with different aspect ratios.

RBC Fixation Protocols

The following procedure outlines the cell fixation protocols for solutions used with RBCs in our succeeding experiments. We prepared a 2.5% glutaraldehyde solution by mixing 1 ml of 25% glutaraldehyde with 9 ml of phosphate-buffered saline (PBS), yielding a total volume of 10 ml. Similarly, we prepared 10 ml of 2% paraformaldehyde solution by combining 5 ml of 4% paraformaldehyde with 5 ml of PBS. The cells were fixed using the 2.5% glutaraldehyde solution with 5 ml of 2% paraformaldehyde for 4 h at 4°C. After fixation, we then washed the solution three times with water, allowing 10 min for each wash on a shaker table. Afterwards, the 4% aqueous osmium tetroxide solution was diluted to 1% solution when mixed with 3 ml of PBS. This 1% osmium tetroxide solution was used for post-fixation in a dark environment within the hood for 100 min. Finally, the solution underwent washing procedures following the same process as described earlier. Both normal oblate-shaped RBCs and abnormal spherical-shaped RBCs generated from normal cells via NaCl treatment were fixed separately to preserve their respective morphologies. Following fixation, the two RBC populations were collected into separate tubes for subsequent analysis. To enable clear differentiation between the cell shapes during fluorescence-based quantification, a shape-specific membrane staining protocol was implemented.⁽⁵⁵⁾ Normal oblate-shaped RBCs were labeled with green fluorescent FITC-dextran (70 kDa, 100 µg/mL), while abnormal spherical-shaped RBCs were stained with red fluorescent with the help of LIVE/DEAD BacLight Bacterial Viability Kit (DMSO 30 µL/mL



and 2 $\mu\text{L}/\text{mL}$ each of the two Invitrogen Live/Dead stains (orange and purple). The kit uses a dye called propidium iodide, which can only enter cells with damaged membranes, causing them to fluoresce red. Since abnormally shaped or damaged RBCs may have compromised membranes, they would also be stained red by this dye. (56) The staining was performed in the dark for 30 min to ensure consistent membrane labeling and minimize photobleaching. This dual-color staining approach allows reliable identification and quantitative comparison of RBCs based on their shape during post-collection fluorescence analysis.

View Article Online
DOI: 10.1039/D6LC00140H

Author contributions

M.S.K.: Writing – original draft (lead); Investigation (lead). M.A.: Investigation (supporting). Y.B.B.: Investigation (supporting). S.J.L.: Conceptualization (supporting); Writing – review & editing (supporting). J.P.: Conceptualization (lead); Funding acquisition (lead); Writing – review & editing (lead).

Conflicts of interest

There are no conflicts to declare.

Data availability

All data reported in this work are available from the corresponding author upon reasonable request.

The supplementary information (SI) associated with this article includes: derivation of the acoustic radiation torque and force along with radiation force function (Y_p); numerical investigation of asymmetric wave scattering from oblate spheroids with varying orientation and aspect ratio; acoustic radiation force factor (F_F) graphs with varying acoustic wave frequency (f) and the PS particle and RBCs diameter (d_p) (Fig. S1); Fig. S2 (supporting experimental results for Fig. 6); Fig. S3 shows S_{11} measurement data of both IDTs by a vector network analyzer; Fig. S4 indicates roles of ART and ARF in particle orientation and particle vertical migration. Supplementary Movie 1 (illustrating movement of spherical and oblate particle in an acoustic field).

Acknowledgements

J.P. acknowledges the National Research Foundation of Korea (NRF) grants funded by the Korea government (MSIT) (Nos. RS-2023-00210891 and RS-2020-NR049568). The microfluidic devices were fabricated by using a mask aligner (MDA-400S, MIDAS) at the Energy Convergence Core Facility at Chonnam National University. S.J.L. acknowledges the support by the National Research Foundation of Korea (NRF-2021R1F1A1063116).

Ethics approval



Ethics approval for the experiments on animal or human subjects reported in the submitted manuscript was obtained. This study was approved by the Institutional Review Board of Chonnam National University (IRB No. 1040198–21701-BR-099–03).

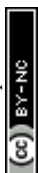
View Article Online
DOI: 10.1039/D6LC00140H

References

- Luciano M, Versaevell M, Vercruyssen E, Procès A, Kalukula Y, Remson A, et al. Appreciating the role of cell shape changes in the mechanobiology of epithelial tissues. *Biophysics Reviews*. 2022;3(1).
- Thon JN, Italiano JE. Platelets: production, morphology and ultrastructure. *Handb Exp Pharmacol*. 2012(210):3-22.
- Byrd BK, Krishnaswamy V, Gui J, Rooney T, Zuurbier R, Rosenkranz K, et al. The shape of breast cancer. *Breast Cancer Res Treat*. 2020;183(2):403-10.
- Kano R. Emergence of Fungal-Like Organisms: Prototheca. *Mycopathologia*. 2020;185(5):747-54.
- Braun-Nesje R, Bertheussen K, Kaplan G, Seljelid R. Salmonid macrophages: Separation, in vitro culture and characterization. *Journal of Fish Diseases*. 2006;4:141-51.
- Ribatti D, Tamma R, Annese T. Epithelial-Mesenchymal Transition in Cancer: A Historical Overview. *Translational Oncology*. 2020;13(6):100773.
- Franchi M, Piperigkou Z, Karamanos K-A, Franchi L, Masola V. Extracellular Matrix-Mediated Breast Cancer Cells Morphological Alterations, Invasiveness, and Microvesicles/Exosomes Release. *Cells*. 2020;9(9):2031.
- Peter Klinken S. Red blood cells. *The International Journal of Biochemistry & Cell Biology*. 2002;34(12):1513-8.
- Ford J. Red blood cell morphology. *International Journal of Laboratory Hematology*. 2013;35(3):351-7.
- Tyrrell L, Rose G, Shukri A, Kahwash SB. Morphologic changes in red blood cells: An illustrated review of clinically important light microscopic findings. *Malays J Pathol*. 2021;43(2):219-39.
- Dasanna AK, Hillringhaus S, Gompper G, Fedosov DA. Effect of malaria parasite shape on its alignment at erythrocyte membrane. *Elife*. 2021;10.
- Perrotta S, Gallagher PG, Mohandas N. Hereditary spherocytosis. *The Lancet*. 2008;372(9647):1411-26.
- Rees DC, Williams TN, Gladwin MT. Sickle-cell disease. *The Lancet*. 2010;376(9757):2018-31.
- Robier C, Klescher D, Reicht G, Amouzadeh-Ghadikolai O, Quehenberger F, Neubauer M. Dacryocytes are a common morphologic feature of autoimmune and microangiopathic haemolytic anaemia. *Clinical Chemistry and Laboratory Medicine (CCLM)*. 2015;53(7):1073-6.
- Diez-Silva M, Dao M, Han J, Lim C-T, Suresh S. Shape and Biomechanical Characteristics of Human Red Blood Cells in Health and Disease. *MRS Bulletin*. 2010;35(5):382-8.
- van Teeseling MCF, de Pedro MA, Cava F. Determinants of Bacterial Morphology: From Fundamentals to Possibilities for Antimicrobial Targeting. *Frontiers in Microbiology*. 2017;8.
- Behdani B, Monjezi S, Carey MJ, Weldon CG, Zhang J, Wang C, et al. Shape-based separation of micro-/nanoparticles in liquid phases. *Biomicrofluidics*. 2018;12(5):051503.



18. Wei Q, Xiong Y, Ma Y, Liu D, Lu Y, Zhang S, et al. High-throughput single-cell assay for precise measurement of the intrinsic mechanical properties and shape characteristics of red blood cells. *Lab on a Chip*. 2024;24(2):305-16. View Article Online DOI: 10.1039/D6LC00140H
19. Khan MS, Julio RH, Ali M, Sachs S, Cierpka C, König J, et al. Microfluidic shape-based separation for cells and particles: recent progress and future perspective. *Lab on a Chip*. 2026.
20. Hur SC, Choi S-E, Kwon S, Carlo DD. Inertial focusing of non-spherical microparticles. *Applied Physics Letters*. 2011;99(4).
21. Li M, Muñoz HE, Goda K, Di Carlo D. Shape-based separation of microalga *Euglena gracilis* using inertial microfluidics. *Scientific Reports*. 2017;7(1):10802.
22. Jiang M, Budzan K, Drazer G. Fractionation by shape in deterministic lateral displacement microfluidic devices. *Microfluidics and Nanofluidics*. 2015;19(2):427-34.
23. Holm SH, Beech JP, Barrett MP, Tegenfeldt JO. Separation of parasites from human blood using deterministic lateral displacement. *Lab on a Chip*. 2011;11(7):1326-32.
24. Matsuda M, Yamada M, Seki M. Blood cell classification utilizing hydrodynamic filtration. *Electronics and Communications in Japan*. 2011;94(1):1-6.
25. Dual J, Hahn P, Leibacher I, Möller D, Schwarz T, Wang J. Acoustofluidics 19: Ultrasonic microrobotics in cavities: devices and numerical simulation. *Lab on a Chip*. 2012;12(20):4010-21.
26. Hahn P, Leibacher I, Baasch T, Dual J. Numerical simulation of acoustofluidic manipulation by radiation forces and acoustic streaming for complex particles. *Lab on a Chip*. 2015;15(22):4302-13.
27. Hahn P, Lamprecht A, Dual J. Numerical simulation of micro-particle rotation by the acoustic viscous torque. *Lab on a Chip*. 2016;16(23):4581-94.
28. Sachs S, Schmidt H, Cierpka C, König J. On the behavior of prolate spheroids in a standing surface acoustic wave field. *Microfluidics and Nanofluidics*. 2023;27(12):81.
29. Chen Y, Ding X, Steven Lin S-C, Yang S, Huang P-H, Nama N, et al. Tunable Nanowire Patterning Using Standing Surface Acoustic Waves. *ACS Nano*. 2013;7(4):3306-14.
30. Khan MS, Ali M, Lee SH, Jang KY, Lee SJ, Park J. Acoustofluidic separation of prolate and spherical micro-objects. *Microsystems & Nanoengineering*. 2024;10(1):6.
31. Ali M, Khan MS, Park J, Zhang C, Park J. Tilted-angle acoustofluidics for particle and cell manipulation: Fundamentals, strategies, and outlook. *Biomedical Instrumentation*. 2026;2(1):100039.
32. Koh J, Kim J, Shin JH, Lee W. Fabrication and integration of microprism mirrors for high-speed three-dimensional measurement in inertial microfluidic system. *Applied Physics Letters*. 2014;105(11).
33. Pasha A, Khasim S, Darwish AAA, Hamdalla TA, Al-Ghamdi SA, Alfadhli S. Flexible, stretchable and electrically conductive PDMS decorated with polypyrrole/manganese-iron oxide nanocomposite as a multifunctional material for high performance EMI shielding applications. *Synthetic Metals*. 2022;283:116984.
34. Park J, Cha B, Almus FG, Sahin MA, Kang H, Kang Y, et al. Acoustic Waves Coupling with Polydimethylsiloxane in Reconfigurable Acoustofluidic Platform. *Advanced Science*. 2024;11(47):2407293.
35. Khan MS, Kim W, Park J. Reconfigurable acoustofluidic platform with vacuum pressure-assisted reversible bonding. *Sensors and Actuators B: Chemical*. 2026;458:139847.
36. Collins DJ, Alan T, Neild A. Particle separation using virtual deterministic lateral displacement (vDLD). *Lab on a Chip*. 2014;14(9):1595-603.
37. Khan MS, Sahin MA, Destgeer G, Park J. Residue-free acoustofluidic manipulation of microparticles via removal of microchannel anechoic corner. *Ultrasonics Sonochemistry*. 2022;89:106161.



38. Pessôa MAS, Neves AAR. Acoustic scattering and forces on an arbitrarily sized fluid sphere by a general acoustic field. *Journal of Sound and Vibration*. 2020;479:115373. View Article Online
DOI: 10.1039/D6LC00140H
39. Leão-Neto JP, Lopes JH, Silva GT. Acoustic radiation torque exerted on a subwavelength spheroidal particle by a traveling and standing plane wave. *J Acoust Soc Am*. 2020;147(4):2177.
40. Mitri FG. Acoustic backscattering and radiation force on a rigid elliptical cylinder in plane progressive waves. *Ultrasonics*. 2016;66:27-33.
41. Fan Z, Mei D, Yang K, Chen Z. Acoustic radiation torque on an irregularly shaped scatterer in an arbitrary sound field. *The Journal of the Acoustical Society of America*. 2008;124(5):2727-32.
42. Mitri FG. Radiation forces and torque on a rigid elliptical cylinder in acoustical plane progressive and (quasi)standing waves with arbitrary incidence. *Physics of Fluids*. 2016;28(7).
43. Wijaya FB, Lim KM. Numerical calculation of acoustic radiation force and torque on non-spherical particles in Bessel beams. *Proceedings of Meetings on Acoustics*. 2016;26(1).
44. Tohme T, Magaud P, Baldas L. Transport of Non-Spherical Particles in Square Microchannel Flows: A Review. *Micromachines*. 2021;12(3):277.
45. Yang S, Kim JY, Lee SJ, Lee SS, Kim JM. Sheathless elasto-inertial particle focusing and continuous separation in a straight rectangular microchannel. *Lab on a Chip*. 2011;11(2):266-73.
46. Kim J, Kim JY, Kim Y, Lee SJ, Kim JM. Shape Measurement of Ellipsoidal Particles in a Cross-Slot Microchannel Utilizing Viscoelastic Particle Focusing. *Analytical Chemistry*. 2017;89(17):8662-6.
47. Ahn SJ, Ahn KH, Lee SJ. Film squeezing process for generating oblate spheroidal particles with high yield and uniform sizes. *Colloid and Polymer Science*. 2016;294(5):859-67.
48. Hoque SZ, Bhattacharyya K, Sen AK. Dynamical motion of an oblate shaped particle exposed to an acoustic standing wave in a microchannel. *Physical Review Fluids*. 2022;7(11):114204.
49. Collins DJ, Alan T, Neild A. The particle valve: On-demand particle trapping, filtering, and release from a microfabricated polydimethylsiloxane membrane using surface acoustic waves. *Applied Physics Letters*. 2014;105(3).
50. Ahmed H, Destgeer G, Park J, Jung JH, Sung HJ. Vertical Hydrodynamic Focusing and Continuous Acoustofluidic Separation of Particles via Upward Migration. *Advanced Science*. 2018;5(2):1700285.
51. Reinhart WH, Piety NZ, Goede JS, Shevkopylas SS. Effect of osmolality on erythrocyte rheology and perfusion of an artificial microvascular network. *Microvascular Research*. 2015;98:102-7.
52. Sesen M, Alan T, Neild A. Microfluidic on-demand droplet merging using surface acoustic waves. *Lab on a Chip*. 2014;14(17):3325-33.
53. Piegols LD, Dwyer T, Glotzer SC, Eniola-Adefeso O. Shape-Dependent Structural Order of Red Blood Cells. *Langmuir*. 2025;41(3):1876-88.
54. Ikumapayi OM, Akinlabi ET, Adeoye AOM, Fatoba SO. Microfabrication and nanotechnology in manufacturing system – An overview. *Materials Today: Proceedings*. 2021;44:1154-62.
55. Dong X, Niu Y, Ding Y, Wang Y, Zhao J, Leng W, et al. Formulation and Drug Loading Features of Nano-Erythrocytes. *Nanoscale Res Lett*. 2017;12(1):202.
56. Boulos L, Prévost M, Barbeau B, Coallier J, Desjardins R. LIVE/DEAD BacLight : application of a new rapid staining method for direct enumeration of viable and total bacteria in drinking water. *J Microbiol Methods*. 1999;37(1):77-86.



Open Access Article. Published on 07 May 2026. Downloaded on 5/8/2026 11:05:46 AM.
This article is licensed under a Creative Commons Attribution-NonCommercial 3.0 Unported Licence.

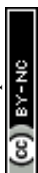
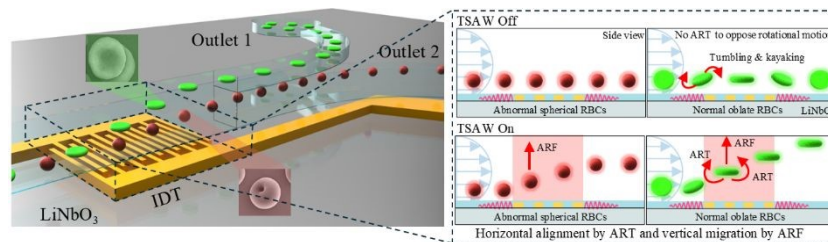


We propose acoustofluidic shape-based separation of oblate spheroids from spheres using traveling surface acoustic wave-induced acoustic radiation torque and force. We demonstrate the label-free separation of the polymer microparticles and red blood cells of spherical and oblate shapes at high purity and recovery rate in a label-free manner.

View Article Online
DOI: 10.1039/D6LC00140H

Muhammad Soban Khan, Mushtaq Ali, Yong Bin Bang, Seong Jae Lee and Jinsoo Park**

Acoustofluidic Separation of Oblate Spheroid from Sphere using Acoustic Radiation Torque and Force



Acoustofluidic Separation of Oblate Spheroid from Sphere using Acoustic Radiation Torque and Force

View Article Online
DOI: 10.1039/C6LC00140H

Muhammad Soban Khan,¹ Mushtaq Ali,¹ Yong Bin Bang,² Seong Jae Lee^{2,*} and Jinsoo Park^{1,*}

¹Department of Mechanical Engineering, Chonnam National University, 77 Yongbong-ro, Buk-gu, Gwangju 61186, Republic of Korea

²Department of Polymer Engineering, The University of Suwon, 17 Wauan-gil, Bongdam-eup, Hwaseong, Gyeonggi 18323, Republic of Korea

*Correspondence: Jinsoo Park (jinsoopark@jnu.ac.kr) and Seong Jae Lee (sjlee@suwon.ac.kr)

Abstract

Cells, bacteria, and other bioparticles exist in diverse shapes, and their morphology plays a pivotal role in biological functions and clinical significance. Various microfluidic approaches have been developed for shape-based separation of bioparticles with the same or similar volume; however, most of them were limited to separation of prolate spheroids from spheres or required a priori labeling and consequent detection. Here, we propose a vertical-type acoustofluidic method for the first separation of oblate spheroid from sphere in a label-free manner. The acoustic radiation torque suppresses the rotational motion of the oblate micro-objects, leading to horizontal alignment with an increase in projected surface area compared to that of the isovolumetric spheres. The enhanced acoustic radiation force, proportional to the projected surface area normal to the wave propagation, allows the oblate spheroids to have greater vertical migration inside a microchannel, resulting in distinct trajectories for the shape-based separation. We conduct numerical simulations of asymmetric wave scattering to elucidate the working principle and experiments to demonstrate the separation of polystyrene microparticles and red blood cells of spherical and oblate shapes at high purity and recovery rate. The proposed acoustofluidic approach holds promise for label-free, shape-based manipulation of bioparticles in cell biology and microbiology.



1. Introduction

View Article Online
DOI: 10.1039/D6LC00140H

Cells, bacteria, and other bioparticles exhibit diverse shapes that significantly influence their biological functions and clinical relevance.(1-4) Human cells exhibit a diverse range of shapes that are crucial for their functions: for instance, immune functions of macrophages,(5) epithelial-to-mesenchymal cancer cell progression,(6) and metastatic potential of tumor cells.(7) Specifically, human red blood cells (RBCs) exhibit a characteristic biconcave shape, with a diameter of 6–8 μm under healthy conditions, which enhances their flexibility and oxygen exchange efficiency.(8, 9) Alterations in RBC morphology are closely associated with pathological conditions, often leading to changes in mechanical properties and reduced oxygen-carrying capacity.(10) For example, malaria-infected RBCs transform from their native biconcave shape into a more spherical form,(11) while hereditary spherocytosis also results in spherical RBCs due to membrane defects.(12) Elongated or elliptical RBCs are associated with elliptocytosis,(10) whereas sickle or crescent-shaped RBCs are characteristic of sickle cell disease.(13) In addition, teardrop-shaped RBCs are indicative of myelofibrosis.(14) Therefore, the ability to identify and separate bioparticles based on shape is of significant importance for biomedical diagnostics, disease monitoring, and therapeutic assessment.(15, 16)

Various microfluidic approaches have been proposed for shape-based bioparticle manipulation with advantages including precise, non-invasive processing, reduced reagent consumption, versatility, and easy integration.(17-19) A few successful demonstrations include inertial microfluidics for separation of spherical and rod-shaped *Euglena gracilis* microalgae,(20, 21) deterministic lateral displacement for separation of biconcave RBCs and elongated *T. cyclops* parasite,(22, 23) and hydrodynamic filtration for separation of erythrocytes blood leukocytes.(24) These approaches primarily rely on flow-induced hydrodynamic effects and often require precise channel geometries or specific flow conditions for effective separation. In contrast, acoustofluidic techniques enable contactless and label-free manipulation of non-spherical particles based on acoustic radiation torque (ART) and acoustic radiation force (ARF), allowing dynamic control over particle orientation and trajectory. In standing bulk acoustic wave(25-27) and standing surface acoustic wave(28, 29) ART has been shown to suppress rotational motion of prolate spheroids, leading to orientation-dependent focusing. Building on this, we previously demonstrated the separation of the prolate spheroids from isovolumetric microspheres in a travelling surface acoustic wave (TSAW) field.(30) However, these approaches have been largely limited to prolate–sphere separation. In such cases, ART-induced alignment reduces the projected surface area, resulting in weaker ARF. In contrast, the present work focuses on oblate spheroids, where alignment increases the projected surface area, leading



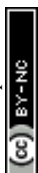
to enhanced ARF and distinct migration behavior. A comprehensive overview of these techniques can be found in our recent review.^(19, 31)

Here, we present a vertical-type acoustofluidic platform that enables, to the best of our knowledge, the first shape-based separation of oblate spheroids from isovolumetric spheres in a contactless and label-free manner, achieved through the combined effects of TSAW-induced ART and ARF. In the vertical-type configuration, the vertical wave propagation, whose magnitude is approximately 2.5 times greater than horizontal counterpart, is primarily utilized for separation of spherical and oblate micro-objects with enhanced separation efficiency and improved operational robustness. The TSAW-induced ART causes horizontal alignment of the oblate spheroids with an increase in the projected surface area normal to the wave propagation. The enhanced ARF on the oblate spheroids in the vertical direction due to the increased projected area allows their trajectory vertically shifted from the trajectory of the microspheres, leading to shape-based separation. We performed numerical simulations of wave scattering from oblate spheroids with varying orientation and aspect ratio (AR) to elucidate that the TSAW-induced ART and ARF are attributed to the asymmetric wave scattering. We also experimentally proved that the acoustic streaming effect is negligible to the acoustofluidic shape-based separation in the proposed platform. Based on the findings, we report the first demonstration of the shape-based separation of oblate and spherical polystyrene (PS) microparticles and RBCs at high purity and recovery rate of ~100%. We expect that the proposed acoustofluidic shape-based separation method holds promise in various fields including cell biology and microbiology.

2. Results and Discussion

2.1 Device configuration

The proposed vertical-type acoustofluidic device consists of a straight interdigital transducer (IDT) on a piezoelectric lithium niobate (LiNbO_3) substrate with a polydimethylsiloxane (PDMS) microchannel with four inlets and two outlets, as shown in Fig. 1a. Suspended particles or cells were introduced through Inlet 1 at a flow rate of 50 $\mu\text{l/hr}$ and directed downward using a vertical sheath flow of 200 $\mu\text{l/hr}$ from Inlet 2, guiding them closer to the IDT. The suspensions were then sandwiched between two additional horizontal sheath flows from Inlets 3 and 4, each at a flow rate of 100 $\mu\text{l/hr}$, to achieve horizontal alignment. Unless otherwise specified, these flow rates were maintained for all experiments, resulting in a throughput of approximately 30–40 cells/s under the present operating conditions. It should be noted that the primary objective of this study is to demonstrate shape-based separation driven by the combined effects of ART



and ARF, rather than to achieve high-throughput performance. The throughput can be further improved through optimization of flow conditions and device design parameters. TSAWs generated by the IDT underneath the microchannel refract into the fluid at the Rayleigh angle ($\sim 22^\circ$ for $\text{LiNbO}_3/\text{water}$ interface), forming leaky longitudinal waves (LWs) within the channel. These acoustic waves induce both ART and ARF, leading to shape-dependent particle behaviors. Specifically, the ART arising from asymmetric side scattering promotes horizontal alignment of oblate spheroids. The ARF originates from asymmetries in forward and backward scattering on the horizontally aligned oblate spheroids (red in Fig. 1b) is greater than that exerted on the spheres (green in Fig. 1b) and thus drives further vertical migration of the oblate particles and cells. For direct observation of the vertical migration, we developed three-dimensional downstream bifurcation, which converts the two vertically distinguished particle trajectories into the horizontal ones. However, because the vertical particle migration is inherently difficult to visualize directly through standard inverted or upright microscopy, we also embedded a prism mirror at the side of the microchannel.(32) This prism optically redirects the side view of the vertical particle trajectories into the microscopes imaging plane, allowing real-time visualization and direct confirmation of the vertical separation process during operation.

For electrical isolation of the fluidic region from the IDT electrodes while preserving acoustic coupling, a thin PDMS membrane is strategically placed between the microchannel and the substrate. This design eliminates direct contact between the fluid and the electrodes, minimizing particle and cell exposure to any residual fringing electric fields.(33) The PDMS insulating properties and dielectric behavior effectively suppress such fields, and the membrane structure provides additional practical advantages: it enables easy replacement of the microfluidic channel while reusing the same substrate, facilitating repeated experiments with consistent acoustic performance.(34, 35) Although minimal residual electric fields may still penetrate, their influence is negligible compared to the acoustic effects, as investigated by Collins et al.,(36) who reported that the TSAW-induced ARF dominates over the accompanying electric forces by several orders of magnitude. This ensures that the observed particle behavior is primarily governed by the acoustic interactions.





Fig. 1. (a) Schematic diagram of the vertical-type acoustofluidic device, (b) Focused image showing a micro-prism for side-view visualization and a downstream vertical bifurcation diverging horizontally into two separate outlets.

2.2 Numerical investigation of asymmetric wave scattering from oblate spheroids with varying orientation and aspect ratio

Our hypothesis for the proposed shape-based separation of oblate spheroids from spheres in the proposed vertical-type acoustofluidic device is that (i) the rotational motion of the oblate spheroids is suppressed by the counter-rotating TSAW-induced ART, leading to horizontal alignment with their minor (shorter) axis (2b) parallel to vertical wave propagation (+z-direction) (Fig. 2a), and (ii) the increased projected area of the horizontally aligned oblate spheroids, perpendicular in the xy -plane in Fig. 1(a), results in an increase in the ARF magnitude, leading to further vertical migration compared to the spheres. For validation, we conducted numerical simulations for the wave scattering from oblate spheroids with varying AR as in Fig. 2. In the numerical calculation, we modeled a spherical PS particle with a diameter of $5\ \mu\text{m}$ and its isovolumetric oblate particles with varying orientation and AR. Incident plane progressive waves are propagating in the +z-direction (from 270° to 90°) with a frequency of 141 MHz to have κ of 1.5 for effective PS particle manipulation by the ARF (ARF factor as a function of κ can be found in Fig. S1).⁽³⁷⁾ Fig. 2a demonstrates our numerical simulation model for acoustic wave scattering from oblate spheroids with varying orientation and AR, defined as the ratio of minor axis (2b) divided by major axis (2a). To isolate the primary vertical component of the leaky LWs, we modeled a +z-propagating plane wave and neglected lateral LW components ($\pm x$ -direction) due to their minimal contribution to vertical migration. The oblate spheroid was placed within a computational domain of radius R_i , surrounded by a perfectly matched layer (PML) (For further details of numerical simulation, see supplementary information).

In our numerical approach, we simplified the phenomenon to focus on the dominant physical mechanisms, namely, the asymmetric wave scattering from oblate spheroids with varying orientation and AR. First, we modeled the fluid as inviscid, thereby neglecting the acoustic streaming effect, induced by wave attenuation due to viscous damping. While acoustic



streaming may be present, its influence on shape-based separation is minimal, as will be explained later with experimental validation (in Section 2.7), because the particle size and wavelength under the operating conditions yield Helmholtz number comparable to 1 (Mie scattering regime) where radiation dominates streaming effects.(38) Second, the assumption of rigid particles provides first-order approximation that captures the essential behavior of shape-induced responses without the added complexity due to deformation. While biological particles like RBCs are indeed deformable, the dominant acoustic interactions, especially at moderate power levels, are primarily governed by geometry rather than minor morphological deformation. Third, the single-particle model neglects the particle-to-particle interactions effect such as secondary ARF. This is a reasonable approximation given the dilute sample conditions used in our experiments to minimize the inter-particle effects. However, we acknowledge that in high-concentration samples (e.g., clinical RBC assays), these effects may become significant and should be addressed in future work. Overall, these assumptions are deliberate, enabling focused investigation of shape-specific ARF and ART without introducing insignificant confounding effects from viscous or collective dynamics.(39)

Fig. 2b shows a polar scattering plot for an oblate spheroid with AR of 0.45 at varying orientation (θ) at a distance of $R_{ext} = 100 \mu\text{m}$. The wave scattering can be classified into forward (90°), backward (270°), and side scattering (0° and 180°). (30, 40) The asymmetry in the side scattering generates an ART on the particle (ART formula available in supplementary information).(41-43) The oblate spheroids exhibit distinct rotational motions, including tumbling, kayaking, and log-rolling. These arise from the velocity gradient in a Poiseuille flow.(44) For $\theta = 0^\circ$ (black), the two components of the side scattering were balanced, and no net torque was induced for the spheroid. On the other hand, for $\theta = 30^\circ$ (red), 45° (blue), and 60° (magenta), the asymmetric side scattering was observed, and the imbalance in the side scattering increased with increasing orientation. These results indicate that the TSAW-induced counter-rotating ART suppresses the rotational motion of the oblate spheroids. As a result, the particles align horizontally with the major axes (2a) aligned with the xy -plane to have $\theta = 0^\circ$ in Fig. 2a. This alignment increases the projected surface area perpendicular to the wave propagation, resulting in the enhanced ARF, which is proportional to the projected surface area, exerted on the oblate objects.

A polar scattering plot for oblate spheroids with varying AR is shown in Fig. 2c. With reference to the sphere with AR = 1.00 (black), the isovolumetric oblate spheroids with AR = 0.45 (red), 0.25 (blue) and 0.18 (magenta) exhibited increasing backward scattering (270°) that is proportional to the ARF magnitude.(40) These results indicate that the magnitude of the ARF



increases as the particle morphology changes from spherical ($AR = 1$) to oblate (smaller AR) and that the horizontally aligned oblate spheroids experience more significant ARF than the isovolumetric spheres. Further details on ARF and ART in terms of wave scattering can be found in supplementary information. As the oblate objects experience a larger magnitude of the ARF compared to the spherical objects with the same volume, we can infer that the oblate spheroids would show further vertical migration than the spheres in the proposed vertical-type acoustofluidic device. This difference in the vertical trajectories of two different shaped isovolumetric micro-objects allows separation at a downstream vertical bifurcation connected to separate outlets (Fig. 1b).



Fig. 2. (a) An oblate spheroid exposed to incident plane progressive waves. Polar scattering plots for oblate spheroids (b) with varying orientation (θ) of 0° , 30° , 45° , and 60° and (b) with varying aspect ratio (AR) of = 1.00, 0.45, 0.25 and 0.18.

2.3 Fabrication of spherical and oblate PS microparticles

For experimental validation of the proposed acoustofluidic approach for the shape-based separation, we first fabricated PS microspheres and transformed them into oblate spheroids with varying AR by film-squeezing. The monodisperse PS spherical microparticles were synthesized by dispersion polymerization,^(45, 46) and the derivate oblate PS microparticles were fabricated by film-squeezing the spherical microparticles.⁽⁴⁷⁾ Further details can be found in Experimental. Fig. 3a–f presents the SEM images of all the fabricated PS particles used in our experiments. The monodispersity of the PS microspheres with a diameter of 5 and 1.2 μm (Fig. 3a and e) was confirmed in the size distribution analysis in Fig. 3g. In the film squeezing process for the morphology transition from spherical to oblate, we varied the film squeezing pressure to fabricate the oblate spheroids with varying AR of 0.45, 0.25, and 0.18 from the 5 μm PS spherical particles and with an AR of 0.18 from the 1.2 μm spherical particles, as shown in Fig. 3b, c, d, and f, respectively. Although the oblate spheroids were found to be slightly polydisperse, compared to the original microspheres, we found that the three kinds of the oblate spheroids had distinct size distributions (Fig. 3g).





Fig. 3. SEM images of the 5 and 1.2 μm -diameter PS particles used in the experiments. (a and e) original microspheres, and oblate spheroids with AR of (b) 0.45, (c) 0.25, (d) 0.18, (f) 0.18 and (g) size distribution of the particles.

2.4 Horizontal alignment of oblate spheroid by acoustic radiation torque

For experimental validation of the horizontal alignment of the oblate spheroids, we examined the orientation of sphere and oblate spheroids before and after the interaction with the TSAW field (Fig. 4 and Supplementary Movie 1). The spheres might rotate in a Poiseuille flow, but their rotational motion cannot be observed due to the geometric symmetry in Fig. 4a and b. Both before and after interaction with the acoustic field, the spheres remained at the same focal. In contrast, the oblate spheroids displayed random orientations and rotational dynamics, mainly kayaking and tumbling, before encountering the acoustic field (Fig. 4c).⁽⁴⁴⁾ These freely rotating oblate particles experienced asymmetric side scattering when exposed to the traveling acoustic field, the rotational motion of the oblate spheroids was suppressed by the ART, resulting in horizontal alignment with their minor axis (2b in Fig. 2a) parallel to the vertical propagation of the leaky LWs (+z-direction), as shown in Fig. 4d. The inset images in Fig. 4d further confirm the horizontal alignment after the oblate spheroids passed through the acoustic field (see also Supplementary Movie 1, corresponding to Fig. 4). The rotational dynamics of oblate particles in acoustic fields have been previously investigated. Hoque et al. reported that oblate particles experience acoustic radiation torque in standing wave fields, which governs their orientation and rotational behavior.⁽⁴⁸⁾ These findings are consistent with our observations, where ART suppresses rotational motion and induces stable horizontal alignment under TSAW excitation. The ART-induced horizontal alignment with major axes (2a in Fig. 2a) in the xy -plane increased the projected surface area normal to the wave propagation, thereby amplifying the net vertical ARF experienced by the oblate objects. As a result, unlike the spheres in Fig. 4a and 4b, the oblate spheroids exhibited a greater vertical migration distance; this increased vertical migration can be substantiated in Fig. 4d, where the oblate spheroids were captured at a higher focal plane approximately 600 μm above the IDT, compared to their



pre-alignment position in Fig. 4c. It should be noted that, although both horizontal and vertical components of the acoustic wave are generated due to leakage at the Rayleigh angle ($\sim 22^\circ$), the vertical component becomes dominant in the present configuration. This is because the surface acoustic wave propagating along the substrate continuously leaks energy into the fluid at an oblique angle, resulting in a significant transfer of momentum in the vertical direction. Additionally, the confinement of the microchannel and the interaction of the leaky wave with the fluid–solid interface enhance upward acoustic radiation effects. As a result, the effective vertical component of the acoustic radiation force is significantly greater (approximately 2.5 times) than the horizontal component, making it the dominant factor governing particle trajectories in this vertical-type acoustofluidic platform. (49, 50)

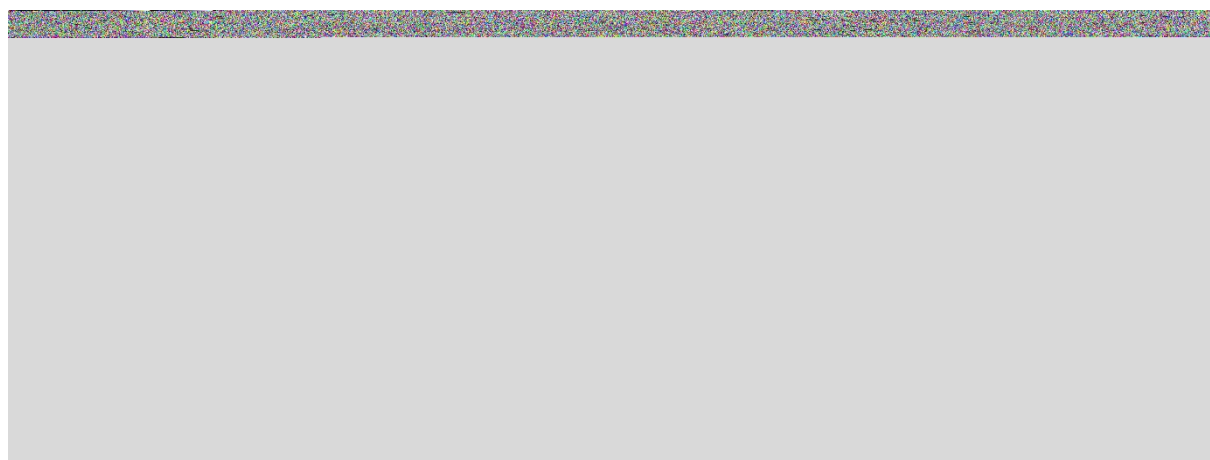


Fig. 4. Microscopic snapshot images of acoustofluidic vertical alignment of (a & b) spherical and (c & d) oblate microparticles.

2.5 Investigation of vertical migration using micro-prism: side-view visualization

The proposed acoustofluidic approach for the shape-based separation of oblate spheroids from spheres is based on varying vertical trajectory depending on the oblate spheroid AR. As the vertical migration of the particles is difficult to observe in the conventional microscopy, we introduced a micro-prism alongside the microchannel for the side-view visualization of the particles, as shown in Fig. 5a. With the side illumination, the scattered fluorescence light can be detected in the microscopy through the mirror side of the prism. (32) As investigated earlier, the oblate particles are horizontally aligned by the ART and migrate vertically by the ARF (Fig. 5b) while the spherical particles only experience the ARF with its magnitude less than that exerted on the oblate ones (Fig. 5c) in the acoustic field. Fig. 5d summarizes the experimental results of the vertical displacement (d_V) as a function of the electrical power (P_e) applied to the IDT for spherical (black) and oblate particles with AR = 0.45 (red), 0.25 (blue), and 0.18 (magenta). Overall, with increasing P_e , the d_V value was measured to increase accordingly due to the increasing ARF magnitude proportional to P_e for all kinds of the particles. As the particle



shape changed from spherical to more oblate (smaller AR), the d_V value increased at the fixed P_e conditions because the ARF magnitude was enhanced by the increased projected area due to the horizontal alignment of the oblate particles caused by the ART.

Fig. 5e–h presents the microscopic side-view images obtained through the prism, showing varying vertical migration of the particles depending on P_e and AR of the PS microparticles. The microchannel had a height of 700 μm with a downstream vertical bifurcation located 500 μm above the microchannel bottom. We confirmed that the side-view visualization of the fluorescent PS microparticles with varying AR can be achieved in our micro-prism-embedded microchannel. From the experimental results, by applying frequency of 141 MHz we found that the lower P_e required for the particles to reach the same d_V tended to decrease with decreasing AR (more oblate). In other words, at the same P_e , the d_V increased with decreasing AR. For example, at $P_e = 30$ mW, the d_V value was measured to be approximately 645, 510, 470, and 390 μm for AR = 0.18 (magenta), 0.25 (blue), 0.45 (red), and 1.00 (black) respectively. With the vertical bifurcation located 500 μm above the microchannel bottom, the oblate particles with AR = 0.18 and 0.25 with d_V greater than 500 μm can be collected in the upper outlet (Outlet 1) while the spherical and oblate particles with AR = 0.45 with d_V smaller than 500 μm can be collected in the lower outlet (Outlet 2), as will be demonstrated later.

Importantly, it should be noted that what enables the proposed shape-based separation is not the absolute value of the vertical migration distance (d_V) but the relative migration difference (Δd_V) between the particle types. In our previous cross-type acoustofluidic platform,⁽³⁰⁾ we observed that the ART suppressed the rotation of prolate spheroids, thereby minimizing their projected area perpendicular to the wave propagation and reducing the ARF magnitude in comparison to the isovolumetric spheres. This enabled label-free separation between spherical and prolate particles, though the difference in lateral migration was limited to approximately 50 μm . In contrast, the proposed vertical configuration aligns the oblate spheroids such that their major axes align perpendicular to the vertical wave propagation, enhancing the interaction mainly with the vertical component of the travelling wave field, which is 2.5 times more significant than the horizontal counterpart due to the Rayleigh angle of 22° at LiNbO₃/water interface. As a consequence, we achieved the vertical migration difference exceeding 100 μm , significantly enhancing separation efficiency and stability (Fig. 5). This enhanced migration not only improves the purity and robustness of particle separation but also offers valuable design insights. In the cross-type acoustofluidic platform, the projected surface area, normal to the horizontal ARF component, remains relatively unchanged between the oblate spheroids and spheres; therefore, these two shapes cannot be effectively distinguished or separated. However,



transitioning from the cross-type to vertical-type configurations addresses this limitation for the previous device, enabling the effective separation of oblate spheroids from spheres, which has remained as an unmet need despite importance and necessity.

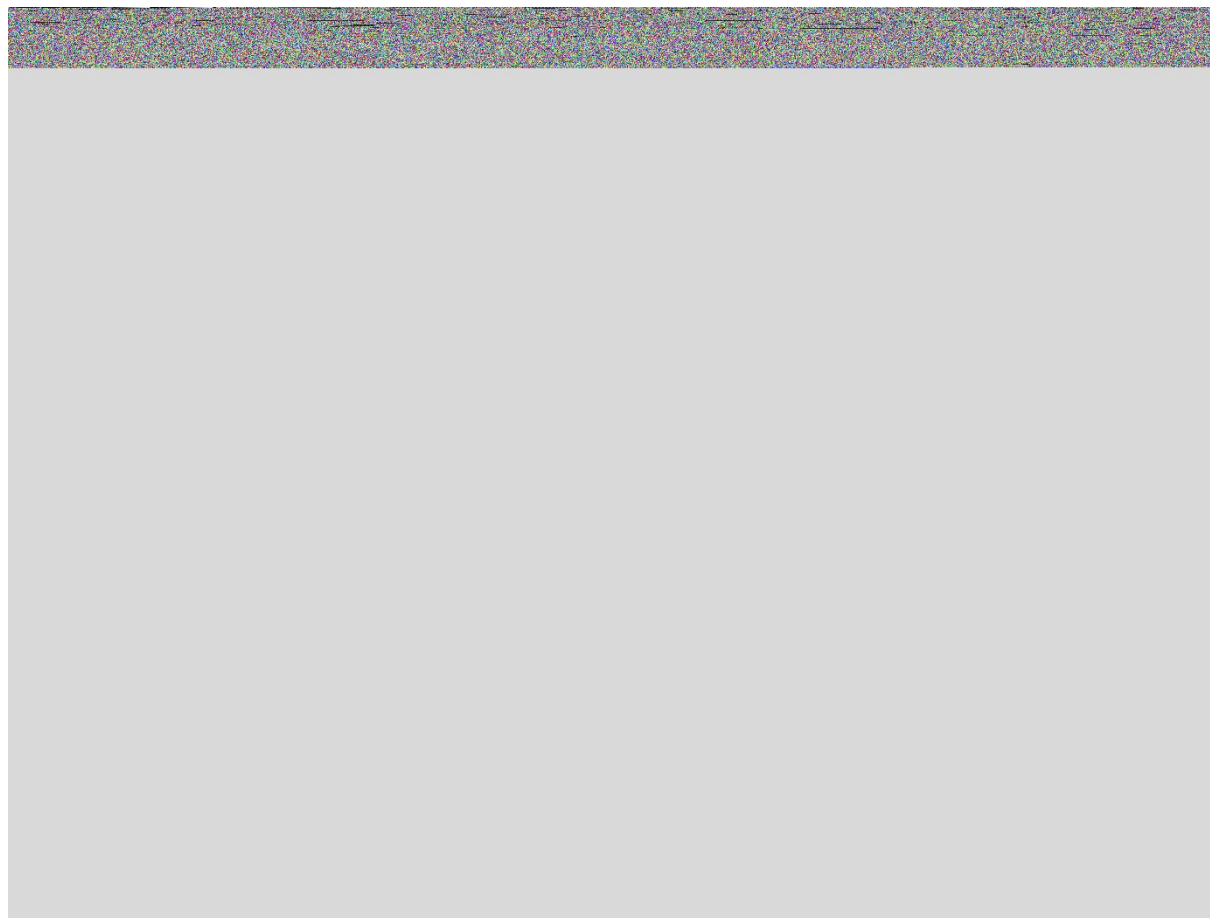


Fig. 5. a) A schematic diagram of the proposed acoustofluidic device with a micro-prism for side-view visualization. Side-view at midstream microchannel for b) oblate and c) spherical particles. d) vertical displacement (d_V) of the particles with varying AR and electrical power (P_e) applied to the IDT. e–h) microscopic prism-view of the different particles.

2.6 Investigation of particle trajectories in a vertical bifurcation microchannel: bottom-view visualization

Fig. 6a–c illustrate the various particle trajectories depending on the particle shape at the downstream vertical bifurcation, connected to upper and lower outlets (Outlets 1 and 2, respectively) for separate collection. In Fig. 5, the vertical displacement by the ARF was measured to be $d_V \cong 190, 260, 260,$ and $310 \mu\text{m}$ at $P_e = 10 \text{ mW}, 395, 470, 510,$ and $643 \mu\text{m}$ at $P_e = 30 \text{ mW}, 660, 665, 690,$ and $700 \mu\text{m}$ at $P_e = 60 \text{ mW}$ for the spherical and oblate particles with $\text{AR} = 1.00$ (black), 0.45 (red), 0.25 (blue), and 0.18 (magenta), respectively. The downstream vertical bifurcation was installed at a height of $500 \mu\text{m}$ inside the microchannel and diverged horizontally into two separate outlets to allow the bottom-view visualization under an inverted microscope. After the bifurcation, the vertically upper channel was connected to the



View Article Online
DOI: 10.1039/D6LC00140H

horizontally upper outlet (Outlet 1) while the vertically lower channel was linked to the horizontally lower outlet (Outlet 2). In the bottom-view visualization (without micro-prism), the varying horizontal trajectory after the vertical bifurcation toward either outlet was observed in Fig. 6d, f, h, and j depending on the particle AR and wave amplitude (P_e applied to the IDT). Without the acoustic field, all the particles were flowing toward the lower outlet after the vertical bifurcation. The collected particle fractions from the two outlets as a function of P_e are shown in Fig. 6e, g, i, and k (black for upper Outlet 1 and red for lower Outlet 2); supplementary Fig. S2 presents fluorescent microscopy images of the green-fluorescent spherical and red-fluorescent oblate PS microparticles collected at Outlet 1 and Outlet 2. At $P_e = 10$ mW, the vertical migration for all the particles was smaller than the vertical bifurcation height, and all the particles were flowing through the lower outlet. On the other hand, at $P_e = 30$ mW, both oblate spheroids with AR = 0.25 and 0.18 showed the vertical migration greater than the vertical bifurcation and thus passed through the upper outlet (Outlet 1) unlike the spherical and oblate particles with AR 0.45. With further increased P_e of 60 mW, all the particles experienced the ARF with a sufficient magnitude to reach the microchannel ceiling and consequently migrated toward the upper outlet. These results suggest that the proposed acoustofluidic platform can be applicable to the shape-based separation of oblate spheroids from spheres depending on the particle shape under the same acoustic field at a fixed P_e condition.

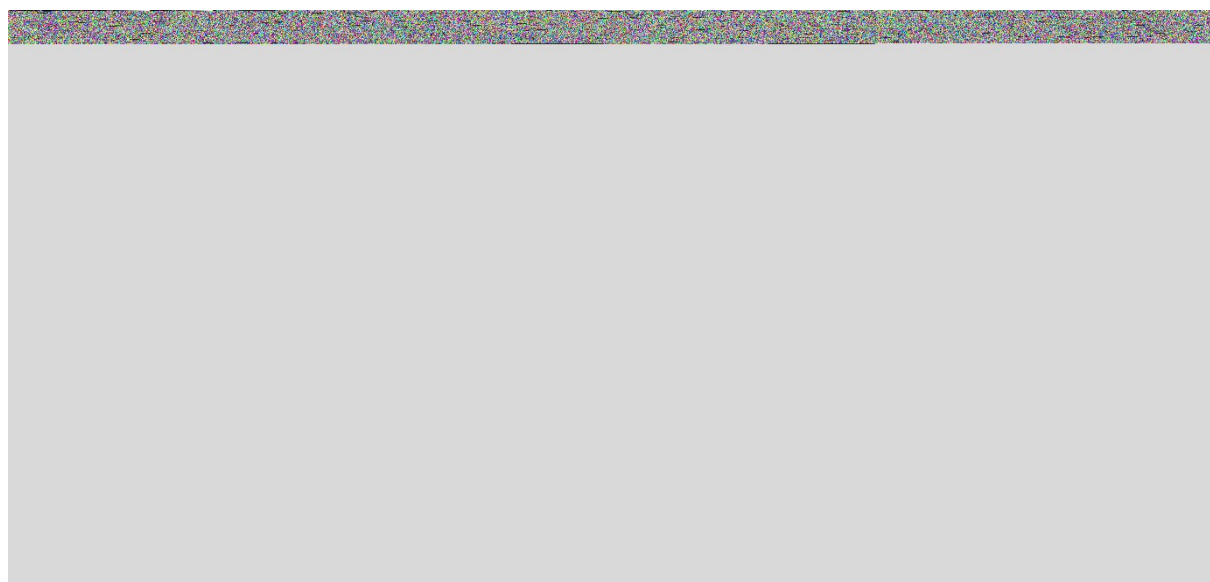


Fig. 6. a–c) Illustrations of the trajectories of spherical and oblate particles in a vertical bifurcation microchannel; d, f, h, and j) Bottom-view visualization of the spherical and oblate PS microparticles with different AR and P_e at the bifurcation. Panels e, g, i, and k show the particle distribution across the two outlets as a function of P_e .

2.7 Acoustofluidic shape-based separation of oblate spheroid from sphere



In the proposed acoustofluidic device with a vertical configuration, we hypothesized that the acoustic streaming effect was negligible to the demonstrated shape-based separation even in a relatively high channel (height of 700 μm) under high-frequency excitation at 141 MHz. This is attributed to our earlier claims that (i) it is not the vertical migration itself but the difference in the vertical migration that enables the proposed shape-based separation in the vertical-type acoustofluidic platform and that (ii) the frequency for separation was carefully chosen such that the scatter size (particles or cells) was comparable to the acoustic wavelength to induce the asymmetric Mie scattering for the ART and ARF acting on the scatter. For validation of our hypothesis, we conducted a negative-control experiment using the isovolumetric spherical ($\sim 1.2 \mu\text{m}$) and oblate (AR of 0.25) particles (green- and red fluorescent in Fig. 7, respectively) with low Helmholtz number. In this Rayleigh scattering regime, as the influence of the acoustic streaming dominated over the acoustic radiation, we could assume that the effects of the TSAW-induced ART and ARF were negligible. In other words, the vertical migration of the particles was solely attributed to the streaming-induced hydrodynamic force. As shown in Fig. 7, we found that both particles were flowing through the lower outlet regardless of the application of the acoustic field. It indicates that the shape-based separation cannot be achieved by the acoustic streaming effect. The acoustic streaming-induced hydrodynamic drag force might cause the vertical migration to some extent; however, it was equal for the particles of both shapes with no noticeable difference in the trajectories even under the elevated P_e condition up to 1.6 W (Fig. 7b), far exceeding the operational level (30 mW) for the radiation-based sorting (Fig. 6). From the observations, we can conclude that the main working principle of the proposed shape-based method is the combined effects of acoustic radiation and torque, not streaming.

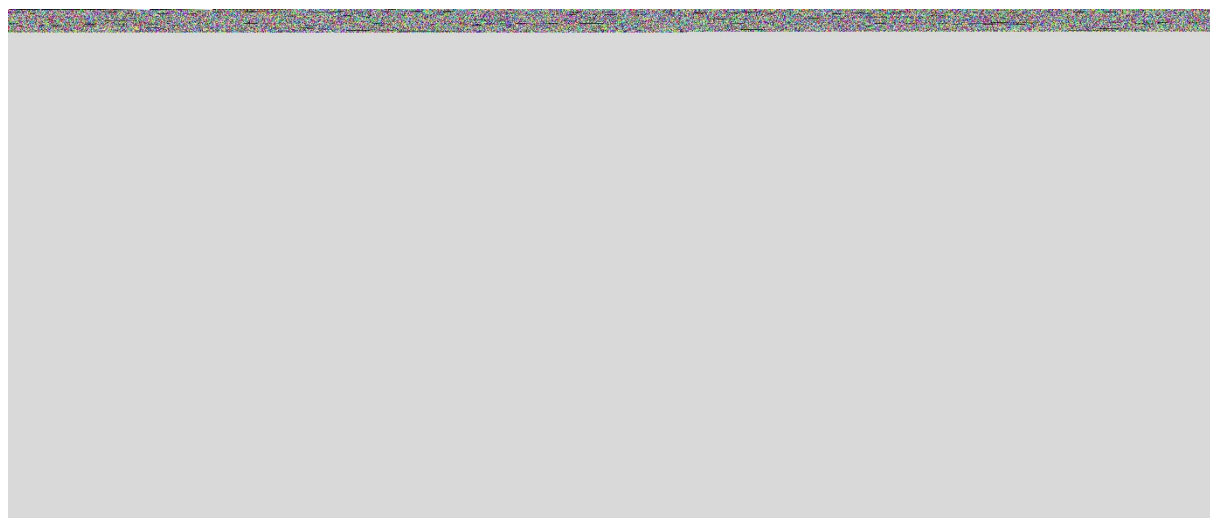


Fig. 7. Acoustofluidic shape-based separation of low Helmholtz number-particles ($\sim 1 \mu\text{m}$) of oblate and spherical shapes (a) without P_e and (b) with P_e .



Building on the numerical and experimental findings, we successfully demonstrated the shape-based separation of the oblate spheroids from the spherical particles in the proposed device in Fig. 8. For clear distinction in the fluorescent images and quantitative analysis of the separation efficiency, we used the red- and green-fluorescent PS microparticles with varying AR; however, this fluorescent labeling is simply for better visualization, not a prerequisite of the proposed label-free acoustofluidic shape-based separation. Fig. 8a demonstrates the acoustofluidic shape-based separation of the red-fluorescent oblate (AR = 0.18) and green-fluorescent spherical PS microparticles at $P_e = 30$ mW. The red oblate particles horizontally aligned by the ART in the acoustic field and experienced greater ARF than the green spherical particles. All the red oblate particles were collected at upper Outlet 1 while all the green spherical particles were retrieved at lower Outlet 2 with 100% purity and recovery rate (Fig. 8d). In Fig. 8b, even with smaller AR difference, the similar results were obtained for the two distinct-shaped particles (red oblate with AR = 0.25 and green spherical) at $P_e = 30$ mW. A reduction in the AR difference led to a slight decrease in the purity of 100% and 92.5% and recovery rate of 96% and 100% for oblate (AR = 0.25) and spherical particles, respectively (Fig. 8e). The proposed acoustofluidic shape-based separation method was found to be applicable to not only between the spherical and oblate particles, but also between the oblate spheroids with different ARs. Fig. 8c shows that the red-fluorescent oblate particles with AR = 0.18 can be separated from the green-fluorescent oblate particles with AR = 0.45 at $P_e = 30$ mW. Both oblate spheroids were horizontally aligned by the ART in the acoustic field. As in our numerical simulation results in Fig. 2c, the more oblate-shaped spheroids (red, AR = 0.18) experienced the greater magnitude of the ARF than less oblate-shaped spheroids (green, AR = 0.45) due to the greater acoustic backward scattering caused by the larger projected surface area. All the red oblate with AR = 0.18 particles were collected at upper Outlet 1 while all the green oblate with AR = 0.48 particles were retrieved at lower Outlet 2 with 100% purity and recovery rate (Fig. 8f). All the results in Fig. 8 were in good agreement in the sorting experiments in Fig. 5 and 6.

View Article Online
DOI: 10.1039/D6LC00140H

Lab on a Chip Accepted Manuscript



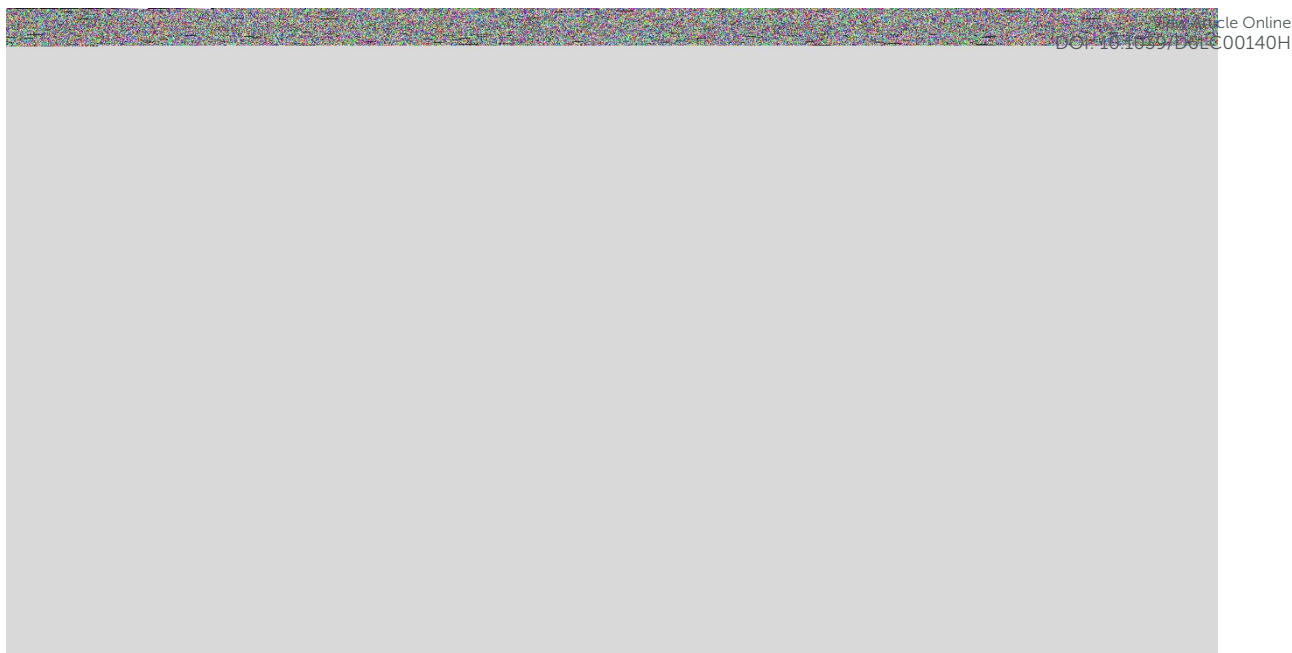
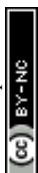


Fig. 8. Acoustofluidic shape-based separation of (a) oblate with AR = 0.18 and spherical, (b) oblate with AR = 0.25 and spherical, and (c) oblate with AR = 0.18 and 0.45. d–f) Purity and recovery rate analysis for the collected particles after separation.

2.8 Acoustofluidic shape-based separation of oblate and spherical RBCs

For validation of the practical applicability, we applied the proposed acoustofluidic approach for separation of oblate and spherical RBCs, as shown in Fig. 9. We modified the normal oblate RBC morphology into the sphere based on osmolarity-dependent shape transition. We used a NaCl solution of 189 mOsm/kg H₂O to achieve the spherical-shaped RBCs without compromising their integrity.⁽⁵¹⁾ We first conducted the RBC sorting experiments separately for the spherical and oblate RBCs, in which the latter samples required the osmolarity-induced RBC shape change. Fig. 9a illustrates the acoustofluidic shape-based RBC separation in the proposed device. The SEM images confirmed the biconcave RBC shape without any treatment (Fig. 9b) and the osmolarity-induced spherical-like RBCs (Fig. 9c), in which the RBC volume remained almost the same. We conducted the RBC sorting experiments with a frequency of 65 MHz tailored to the RBC properties (details can be found in Fig. S2). Fig. 9d shows the varying trajectory of the morphology-altered spherical RBCs at the vertical bifurcation depending on P_e applied to the IDT. Due to the spherical shape, the abnormal RBCs experienced comparably less ARF and thus flowed toward the lower outlet until $P_e = 50$ mW. With the increased P_e of 70 mW, the spherical RBCs vertically migrated further than 500 μm and thus were collected at the upper Outlet 1. On the other hand, the biconcave normal RBCs in Fig. 9e experienced the TSAW-induced ART due to the asymmetric side scattering, leading to the horizontal RBC



alignment. The increased projected surface area caused the ARF acting on them to increase so that their vertical migration was greater than that of the spherical RBCs at the same acoustic intensity conditions. The vertical trajectory transition of the normal RBCs was observed at $P_e = 30$ mW, lower than the threshold power required for the spherical RBCs ($P_e = 70$ mW in Fig. 9d).

Following the sorting experiments, we conducted the simultaneous separation experiments using mixed populations of spherical and oblate, disc-shaped RBCs, as shown in Fig. 9f. Until low P_e applied to the transducer up to 20 mW, neither spherical nor oblate RBCs experienced sufficient ARF to have a vertical migration exceeding 500 μm (location of the vertical bifurcation at downstream). Both-shaped RBCs were collected from the lower outlet (Outlet 2), as can be expected from the independent sorting experiment results. Upon increasing the power up to 30 mW, significant ARF was exerted on the horizontally oriented oblate RBCs, leading to their trajectories translocated to the upper outlet (Outlet 1), separated from the spherical RBCs. At $P_e = 50$ mW, even a few non-target spherical RBCs exhibited sufficient vertical migration and passed through the upper outlet, together with the oblate RBCs. At $P_e = 70$ mW, both oblate and spherical RBCs experienced significant ARF and thus vertically migrated into the upper Outlet 1.

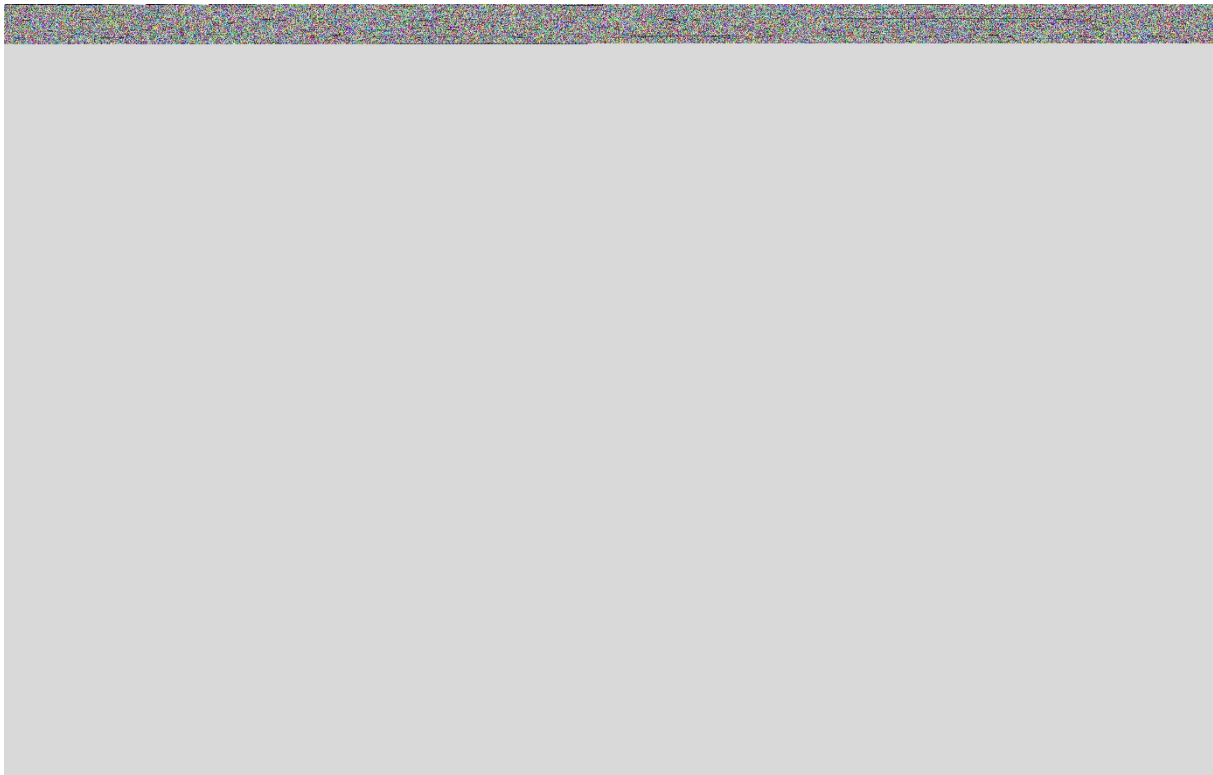


Fig. 9. a) Schematic of vertical-type acoustofluidic device for the shape-based RBCs sorting. Scanning electron micrographs of b) normal biconcave-shaped RBCs prior to osmotic treatment, and (c) RBCs in hypotonic solution (189 mOsm/kg H_2O). RBC sorting images for (d) spherical-shaped and (e) biconcave-shaped RBCs at varying P_e .



For quantitative evaluation of the shape-based RBC separation efficiency, we utilized the fluorescence-labeled RBCs (oblate in green and spherical in red) even though the proposed acoustofluidic approach does not require any label for separation. The labeling did not affect cell morphology or behavior but enabled fluorescence-based analysis of the RBCs with two different shapes. Fig. 10 shows the purity of the collected abnormal spherical and normal oblate RBCs at both outlets at varying P_e applied to the transducer. For quantification, we calculated the purity by assuming the oblate and spherical RBCs as the targets for the upper and lower outlets, respectively. From P_e of 0 to 20 mW, the purity of the abnormal RBCs was 50% as both-shaped RBCs were all collected in the lower outlet (Fig. 10a–c). At $P_e = 30$ mW, the purity of the normal RBCs with green fluorescence at Outlet 1 was 100% while that of the abnormal RBCs with red fluorescence at Outlet 2 was 86%, indicating a few oblate RBCs remained with the spherical RBCs (Fig. 10d). This impurity may be attributed to the non-uniformity of the normal RBCs in size and shape, as in Fig. 9b. With the elevated power of 50 mW, on the other hand, the purity of the abnormal, spherical RBCs increased to 100% while that of the normal, oblate RBCs reduced to 90% since a few spherical RBCs vertically migrated to the upper outlet (Fig. 10e) due to the polydispersity in shape and size, as in Fig. 9c. At $P_e = 70$ mW, the purity of the normal RBCs was 50% as all the RBCs were collected in upper outlet (Fig. 10f). These results underscore the importance of the optimization of the operating conditions, especially P_e , for efficient acoustofluidic shape-based separation. It should be highlighted that the proposed acoustofluidic device in the vertical configuration enables the first demonstration of the RBC separation based on the cell morphology in a label-free manner.

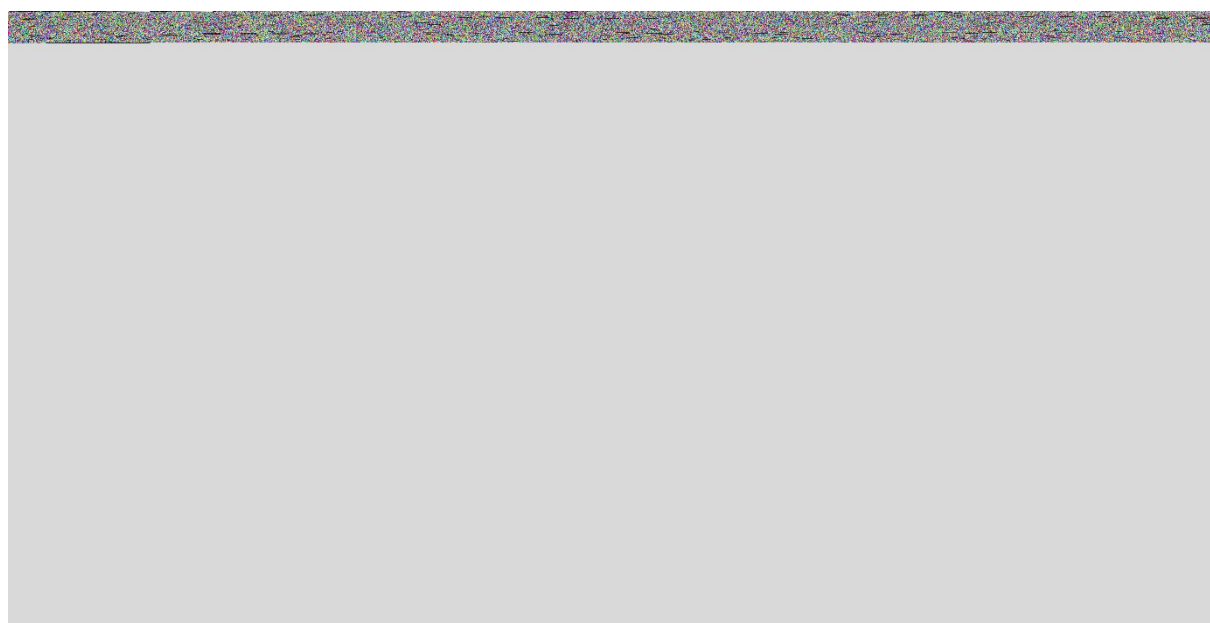


Fig. 10. (a–f) Quantitative evaluation of the shape-based RBC separation by collected samples at the outlets at different P_e with their purity at each outlet. Article Online
DOI: 10.1039/D6LC00140H

It is worth noting that, the magnitude of ARF exerted on an object is proportional to the wave amplitude squared and also electrical power applied to the transducer,(52) regardless of acoustic frequency. In our experiments, we used the 5 μm spherical PS particles and their derivative isovolumetric oblate particles with varying aspect ratio whereas the normal oblate RBC size ranged from 6 to 8 μm under healthy conditions. The non-uniform size distribution of the oblate particles (Fig. 3g) and RBCs (Fig. 9b and 9c) might have reduced the separation efficiency in the experimental demonstrations. Moreover, in Fig. 8, the separation of isovolumetric oblate and spherical PS particles were achieved at P_e of 30 mW. On the contrary, in Fig. 10, we applied comparable or larger P_e for separation of the oblate and spherical RBCs although the RBC size was larger than the PS particles. This can be attributed to the reduced difference in acoustic impedance contrast for the RBCs compared to the PS microparticles. As the acoustic impedance contrast at the RBC/water interface was smaller than that at the PS particle/water, the higher electrical power would have been applied for the shape-based RBC separation.

It is important to note that healthy RBCs typically exhibit a relatively uniform biconcave (discocyte) morphology with limited variation in aspect ratio under physiological conditions. In contrast, under pathological conditions such as hereditary spherocytosis, RBCs transform from biconcave discocytes into near-spherical spherocytes due to membrane loss and structural alterations, resulting in a significant reduction in shape anisotropy.(53) In this study, spherical particles are used as representative models for such abnormal RBC morphologies. Therefore, the proposed method is particularly suited for separating particles with pronounced shape differences, while separation of subtle variations within healthy RBC populations is beyond the scope of the present work.

3. Conclusions

We developed an acoustofluidic platform in the vertical configuration for shape-based separation of the oblate spheroids from spheres in a label free manner based on the TASW-induced ART and ARF. Our numerical and experimental investigations revealed that asymmetric side scattering exerts a counterrotating ART on the oblate particles, repressing the rotation of the oblate objects and thus aligning their shorter, minor axis parallel to the wave propagation. This horizontal alignment increases the projected surface area of the oblate spheroids to the vertical wave propagation, enhancing backward scattering and amplifying the ARF. The increased ARF acting on the oblate micro-objects allows them to have further vertical



migration than the isovolumetric spherical ones. Based on these findings, we successfully demonstrated the shape-based separation of the spherical and oblate PS microparticles and RBCs at high purity and recovery rate.

4. Experimental

Microfluidic Device

The IDT composed of a bimetallic layer of Cr and Au (thickness of 20 and 100 nm, respectively) were deposited on a 500 μm -thick 128°-rotated, Y-cut, X-propagating LiNbO₃ substrate (MTI Korea) by means of the photolithography, E-beam evaporation, and lift-off procedure.⁽⁵⁴⁾ Two set of IDTs were utilized in the experiments, one having comb-shaped electrode spacing ($\lambda/4$) of 7 μm and other with a comb-shaped electrode spacing ($\lambda/4$) of 15.2 μm with a total aperture of 1 mm and consists of 30 electrode pairs. A vector network analyzer (E5071B, Agilent Technologies) was used to determine the resonant frequency of the straight IDTs as 141 MHz and 65 MHz respectively. A Fig. S3 shows the S_{11} measurement data of both IDTs by a vector network analyzer. For applications of RF AC signals to the straight IDT, an RF signal generator (BSG F10, Belektronig GmbH) was used. To fabricate the bifurcated rectangular PDMS microchannel, the 3D mold was created with 3D printer and then the soft lithography process was performed to create 3D microchannel. The mold was pre-treated with 1H, 1H, 2H, and 2H-Perfluorooctyltriethoxysilane (Sigma-Aldrich) before pouring the PDMS mixture (Sylgard 184A and 184B, Dow Corning) on it. The rectangular microchannel had a height (h) of 700 μm and a width (w) of 300 μm . The micro-prism of 2 mm \times 2 mm (N-BK7 Right Angle Prism, Edmund Optics Worldwide) was placed on the side of the microchannel 2 mm away from the microchannel wall. After fabricating the prism-embedded microchannel, the microchannel chip was bonded to the substrate using oxygen plasma treatment (Covance, Femto Science). Fluorescent PS microspheres with a diameter of 5 μm were sourced from (Thermo Scientific, Inc.). The sample and sheath fluid were injected into the microchannel using a syringe pump (neMESYS Cetoni GmbH), with particles suspended in distilled water (Dyne Bio Inc). For observe the behavior of the particles, we used a high-speed CMOS camera (VEO 710L, Phantom) paired with an inverted microscope (IX73, Olympus).

Microparticle Fabrication

Fabricating PS spherical microparticles with a diameter of 5 μm , 1.6 g of polyvinylpyrrolidone (PVP, Sigma-Aldrich) was first dissolved in 210 g of butanol and magnetically stirred for 1 h. The butanol solution containing PVP was added to a 40 g solution of styrene monomer



containing 0.4 g of azobisisobutyronitrile (AIBN) in a 500 ml three-necked double-jacket reactor equipped with a reflux condenser, and then polymerization was initiated. The polymerization was performed at 70°C and 120 rpm for 24 h under N₂ atmosphere. Generating oblate microparticles, polyvinyl alcohol (PVA) (Sigma-Aldrich) was used to prepare a polymer film containing monodisperse PS spherical microparticles for uniaxial squeezing. First, 7.5 g of PVA was added to 150 ml of distilled water at 80°C and sufficiently dissolved using magnetic stirring for 4-5 h. 0.1 wt% of PS spherical microparticles were added to this PVA aqueous solution. The uniformly dispersed mixture was poured onto a flat aluminum tray and dried to obtain a flexible PVA film containing PS spherical microparticles. Fabrication of oblate microparticles, the film was cut into a circular shape and was placed between two silicone rubber sheets (HSW Co., South Korea) to form a three-layered composite. The composite consisting of these three layers was uniaxially squeezed using a press at 135°C with a compression range of 17–83%. The squeezed film with different degrees of compression were dissolved in distilled water at 80°C and then centrifuged to recover the PS oblate microparticles with different aspect ratios.

RBC Fixation Protocols

The following procedure outlines the cell fixation protocols for solutions used with RBCs in our succeeding experiments. We prepared a 2.5% glutaraldehyde solution by mixing 1 ml of 25% glutaraldehyde with 9 ml of phosphate-buffered saline (PBS), yielding a total volume of 10 ml. Similarly, we prepared 10 ml of 2% paraformaldehyde solution by combining 5 ml of 4% paraformaldehyde with 5 ml of PBS. The cells were fixed using the 2.5% glutaraldehyde solution with 5 ml of 2% paraformaldehyde for 4 h at 4°C. After fixation, we then washed the solution three times with water, allowing 10 min for each wash on a shaker table. Afterwards, the 4% aqueous osmium tetroxide solution was diluted to 1% solution when mixed with 3 ml of PBS. This 1% osmium tetroxide solution was used for post-fixation in a dark environment within the hood for 100 min. Finally, the solution underwent washing procedures following the same process as described earlier. Both normal oblate-shaped RBCs and abnormal spherical-shaped RBCs generated from normal cells via NaCl treatment were fixed separately to preserve their respective morphologies. Following fixation, the two RBC populations were collected into separate tubes for subsequent analysis. To enable clear differentiation between the cell shapes during fluorescence-based quantification, a shape-specific membrane staining protocol was implemented.⁽⁵⁵⁾ Normal oblate-shaped RBCs were labeled with green fluorescent FITC-dextran (70 kDa, 100 µg/mL), while abnormal spherical-shaped RBCs were stained with red fluorescent with the help of LIVE/DEAD BacLight Bacterial Viability Kit (DMSO 30 µL/mL



and 2 $\mu\text{L}/\text{mL}$ each of the two Invitrogen Live/Dead stains (orange and purple). The kit uses a dye called propidium iodide, which can only enter cells with damaged membranes, causing them to fluoresce red. Since abnormally shaped or damaged RBCs may have compromised membranes, they would also be stained red by this dye. (56) The staining was performed in the dark for 30 min to ensure consistent membrane labeling and minimize photobleaching. This dual-color staining approach allows reliable identification and quantitative comparison of RBCs based on their shape during post-collection fluorescence analysis.

View Article Online
DOI: 10.1039/D6LC00140H

Author contributions

M.S.K.: Writing – original draft (lead); Investigation (lead). M.A.: Investigation (supporting). Y.B.B.: Investigation (supporting). S.J.L.: Conceptualization (supporting); Writing – review & editing (supporting). J.P.: Conceptualization (lead); Funding acquisition (lead); Writing – review & editing (lead).

Conflicts of interest

There are no conflicts to declare.

Data availability

All data reported in this work are available from the corresponding author upon reasonable request.

The supplementary information (SI) associated with this article includes: derivation of the acoustic radiation torque and force along with radiation force function (Y_p); numerical investigation of asymmetric wave scattering from oblate spheroids with varying orientation and aspect ratio; acoustic radiation force factor (F_F) graphs with varying acoustic wave frequency (f) and the PS particle and RBCs diameter (d_p) (Fig. S1); Fig. S2 (supporting experimental results for Fig. 6); Fig. S3 shows S_{11} measurement data of both IDTs by a vector network analyzer; Fig. S4 indicates roles of ART and ARF in particle orientation and particle vertical migration. Supplementary Movie 1 (illustrating movement of spherical and oblate particle in an acoustic field).

Acknowledgements

J.P. acknowledges the National Research Foundation of Korea (NRF) grants funded by the Korea government (MSIT) (Nos. RS-2023-00210891 and RS-2020-NR049568). The microfluidic devices were fabricated by using a mask aligner (MDA-400S, MIDAS) at the Energy Convergence Core Facility at Chonnam National University. S.J.L. acknowledges the support by the National Research Foundation of Korea (NRF-2021R1F1A1063116).

Ethics approval



All procedures performed in this study were conducted in accordance with the Bioethics and Safety Act of the Republic of Korea and the ethical principles outlined in the Declaration of Helsinki. The study also follows the guidelines of Chonnam National University and complies with Korean Good Clinical Practice (KGCP) and International Council for Harmonisation (ICH) standards. This study was reviewed and approved by the Institutional Review Board (IRB) of Chonnam National University (IRB No. 1040198-230705-BR-085-03). The requirement for informed consent was waived by the IRB due to the exclusive use of fully anonymized human-derived samples, with no identifiable personal information involved.

References

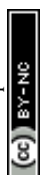
1. Luciano M, Versaevel M, Vercruyse E, Procès A, Kalukula Y, Remson A, et al. Appreciating the role of cell shape changes in the mechanobiology of epithelial tissues. *Biophysics Reviews*. 2022;3(1).
2. Thon JN, Italiano JE. Platelets: production, morphology and ultrastructure. *Handb Exp Pharmacol*. 2012(210):3-22.
3. Byrd BK, Krishnaswamy V, Gui J, Rooney T, Zurbier R, Rosenkranz K, et al. The shape of breast cancer. *Breast Cancer Res Treat*. 2020;183(2):403-10.
4. Kano R. Emergence of Fungal-Like Organisms: Prototheca. *Mycopathologia*. 2020;185(5):747-54.
5. Braun-Nesje R, Bertheussen K, Kaplan G, Seljelid R. Salmonid macrophages: Separation, in vitro culture and characterization. *Journal of Fish Diseases*. 2006;4:141-51.
6. Ribatti D, Tamma R, Annese T. Epithelial-Mesenchymal Transition in Cancer: A Historical Overview. *Translational Oncology*. 2020;13(6):100773.
7. Franchi M, Piperigkou Z, Karamanos K-A, Franchi L, Masola V. Extracellular Matrix-Mediated Breast Cancer Cells Morphological Alterations, Invasiveness, and Microvesicles/Exosomes Release. *Cells*. 2020;9(9):2031.
8. Peter Klinken S. Red blood cells. *The International Journal of Biochemistry & Cell Biology*. 2002;34(12):1513-8.
9. Ford J. Red blood cell morphology. *International Journal of Laboratory Hematology*. 2013;35(3):351-7.
10. Tyrrell L, Rose G, Shukri A, Kahwash SB. Morphologic changes in red blood cells: An illustrated review of clinically important light microscopic findings. *Malays J Pathol*. 2021;43(2):219-39.
11. Dasanna AK, Hillringhaus S, Gompper G, Fedosov DA. Effect of malaria parasite shape on its alignment at erythrocyte membrane. *Elife*. 2021;10.
12. Perrotta S, Gallagher PG, Mohandas N. Hereditary spherocytosis. *The Lancet*. 2008;372(9647):1411-26.
13. Rees DC, Williams TN, Gladwin MT. Sickle-cell disease. *The Lancet*. 2010;376(9757):2018-31.
14. Robier C, Klescher D, Reicht G, Amouzadeh-Ghadikolai O, Quehenberger F, Neubauer M. Dacryocytes are a common morphologic feature of autoimmune and microangiopathic haemolytic anaemia. *Clinical Chemistry and Laboratory Medicine (CCLM)*. 2015;53(7):1073-6.
15. Diez-Silva M, Dao M, Han J, Lim C-T, Suresh S. Shape and Biomechanical Characteristics of Human Red Blood Cells in Health and Disease. *MRS Bulletin*. 2010;35(5):382-8.



16. van Teeseling MCF, de Pedro MA, Cava F. Determinants of Bacterial Morphology From Fundamentals to Possibilities for Antimicrobial Targeting. *Frontiers in Microbiology*. 2017;8. View Article Online
DOI: 10.1039/7D6LC00140H
17. Behdani B, Monjezi S, Carey MJ, Weldon CG, Zhang J, Wang C, et al. Shape-based separation of micro-/nanoparticles in liquid phases. *Biomicrofluidics*. 2018;12(5):051503.
18. Wei Q, Xiong Y, Ma Y, Liu D, Lu Y, Zhang S, et al. High-throughput single-cell assay for precise measurement of the intrinsic mechanical properties and shape characteristics of red blood cells. *Lab on a Chip*. 2024;24(2):305-16.
19. Khan MS, Julio RH, Ali M, Sachs S, Cierpka C, König J, et al. Microfluidic shape-based separation for cells and particles: recent progress and future perspective. *Lab on a Chip*. 2026.
20. Hur SC, Choi S-E, Kwon S, Carlo DD. Inertial focusing of non-spherical microparticles. *Applied Physics Letters*. 2011;99(4).
21. Li M, Muñoz HE, Goda K, Di Carlo D. Shape-based separation of microalga *Euglena gracilis* using inertial microfluidics. *Scientific Reports*. 2017;7(1):10802.
22. Jiang M, Budzan K, Drazer G. Fractionation by shape in deterministic lateral displacement microfluidic devices. *Microfluidics and Nanofluidics*. 2015;19(2):427-34.
23. Holm SH, Beech JP, Barrett MP, Tegenfeldt JO. Separation of parasites from human blood using deterministic lateral displacement. *Lab on a Chip*. 2011;11(7):1326-32.
24. Matsuda M, Yamada M, Seki M. Blood cell classification utilizing hydrodynamic filtration. *Electronics and Communications in Japan*. 2011;94(1):1-6.
25. Dual J, Hahn P, Leibacher I, Möller D, Schwarz T, Wang J. Acoustofluidics 19: Ultrasonic microrobotics in cavities: devices and numerical simulation. *Lab on a Chip*. 2012;12(20):4010-21.
26. Hahn P, Leibacher I, Baasch T, Dual J. Numerical simulation of acoustofluidic manipulation by radiation forces and acoustic streaming for complex particles. *Lab on a Chip*. 2015;15(22):4302-13.
27. Hahn P, Lamprecht A, Dual J. Numerical simulation of micro-particle rotation by the acoustic viscous torque. *Lab on a Chip*. 2016;16(23):4581-94.
28. Sachs S, Schmidt H, Cierpka C, König J. On the behavior of prolate spheroids in a standing surface acoustic wave field. *Microfluidics and Nanofluidics*. 2023;27(12):81.
29. Chen Y, Ding X, Steven Lin S-C, Yang S, Huang P-H, Nama N, et al. Tunable Nanowire Patterning Using Standing Surface Acoustic Waves. *ACS Nano*. 2013;7(4):3306-14.
30. Khan MS, Ali M, Lee SH, Jang KY, Lee SJ, Park J. Acoustofluidic separation of prolate and spherical micro-objects. *Microsystems & Nanoengineering*. 2024;10(1):6.
31. Ali M, Khan MS, Park J, Zhang C, Park J. Tilted-angle acoustofluidics for particle and cell manipulation: Fundamentals, strategies, and outlook. *Biomedical Instrumentation*. 2026;2(1):100039.
32. Koh J, Kim J, Shin JH, Lee W. Fabrication and integration of microprism mirrors for high-speed three-dimensional measurement in inertial microfluidic system. *Applied Physics Letters*. 2014;105(11).
33. Pasha A, Khasim S, Darwish AAA, Hamdalla TA, Al-Ghamdi SA, Alfadhli S. Flexible, stretchable and electrically conductive PDMS decorated with polypyrrole/manganese-iron oxide nanocomposite as a multifunctional material for high performance EMI shielding applications. *Synthetic Metals*. 2022;283:116984.
34. Park J, Cha B, Almus FG, Sahin MA, Kang H, Kang Y, et al. Acoustic Waves Coupling with Polydimethylsiloxane in Reconfigurable Acoustofluidic Platform. *Advanced Science*. 2024;11(47):2407293.
35. Khan MS, Kim W, Park J. Reconfigurable acoustofluidic platform with vacuum pressure-assisted reversible bonding. *Sensors and Actuators B: Chemical*. 2026;458:139847.



36. Collins DJ, Alan T, Neild A. Particle separation using virtual deterministic lateral displacement (vDLD). *Lab on a Chip*. 2014;14(9):1595-603. View Article Online
DOI: 10.1039/D4LC00140H
37. Khan MS, Sahin MA, Destgeer G, Park J. Residue-free acoustofluidic manipulation of microparticles via removal of microchannel anechoic corner. *Ultrasonics Sonochemistry*. 2022;89:106161.
38. Pessôa MAS, Neves AAR. Acoustic scattering and forces on an arbitrarily sized fluid sphere by a general acoustic field. *Journal of Sound and Vibration*. 2020;479:115373.
39. Leão-Neto JP, Lopes JH, Silva GT. Acoustic radiation torque exerted on a subwavelength spheroidal particle by a traveling and standing plane wave. *J Acoust Soc Am*. 2020;147(4):2177.
40. Mitri FG. Acoustic backscattering and radiation force on a rigid elliptical cylinder in plane progressive waves. *Ultrasonics*. 2016;66:27-33.
41. Fan Z, Mei D, Yang K, Chen Z. Acoustic radiation torque on an irregularly shaped scatterer in an arbitrary sound field. *The Journal of the Acoustical Society of America*. 2008;124(5):2727-32.
42. Mitri FG. Radiation forces and torque on a rigid elliptical cylinder in acoustical plane progressive and (quasi)standing waves with arbitrary incidence. *Physics of Fluids*. 2016;28(7).
43. Wijaya FB, Lim KM. Numerical calculation of acoustic radiation force and torque on non-spherical particles in Bessel beams. *Proceedings of Meetings on Acoustics*. 2016;26(1).
44. Tohme T, Magaud P, Baldas L. Transport of Non-Spherical Particles in Square Microchannel Flows: A Review. *Micromachines*. 2021;12(3):277.
45. Yang S, Kim JY, Lee SJ, Lee SS, Kim JM. Sheathless elasto-inertial particle focusing and continuous separation in a straight rectangular microchannel. *Lab on a Chip*. 2011;11(2):266-73.
46. Kim J, Kim JY, Kim Y, Lee SJ, Kim JM. Shape Measurement of Ellipsoidal Particles in a Cross-Slot Microchannel Utilizing Viscoelastic Particle Focusing. *Analytical Chemistry*. 2017;89(17):8662-6.
47. Ahn SJ, Ahn KH, Lee SJ. Film squeezing process for generating oblate spheroidal particles with high yield and uniform sizes. *Colloid and Polymer Science*. 2016;294(5):859-67.
48. Hoque SZ, Bhattacharyya K, Sen AK. Dynamical motion of an oblate shaped particle exposed to an acoustic standing wave in a microchannel. *Physical Review Fluids*. 2022;7(11):114204.
49. Collins DJ, Alan T, Neild A. The particle valve: On-demand particle trapping, filtering, and release from a microfabricated polydimethylsiloxane membrane using surface acoustic waves. *Applied Physics Letters*. 2014;105(3).
50. Ahmed H, Destgeer G, Park J, Jung JH, Sung HJ. Vertical Hydrodynamic Focusing and Continuous Acoustofluidic Separation of Particles via Upward Migration. *Advanced Science*. 2018;5(2):1700285.
51. Reinhart WH, Piety NZ, Goede JS, Shevkopyas SS. Effect of osmolality on erythrocyte rheology and perfusion of an artificial microvascular network. *Microvascular Research*. 2015;98:102-7.
52. Sesen M, Alan T, Neild A. Microfluidic on-demand droplet merging using surface acoustic waves. *Lab on a Chip*. 2014;14(17):3325-33.
53. Piegols LD, Dwyer T, Glotzer SC, Eniola-Adefeso O. Shape-Dependent Structural Order of Red Blood Cells. *Langmuir*. 2025;41(3):1876-88.
54. Ikumapayi OM, Akinlabi ET, Adeoye AOM, Fatoba SO. Microfabrication and nanotechnology in manufacturing system – An overview. *Materials Today: Proceedings*. 2021;44:1154-62.



55. Dong X, Niu Y, Ding Y, Wang Y, Zhao J, Leng W, et al. Formulation and Drug Loading Features of Nano-Erythrocytes. *Nanoscale Res Lett.* 2017;12(1):202. [View Article Online](#)
DOI: 10.1039/D6LC00140H
56. Boulos L, Prévost M, Barbeau B, Coallier J, Desjardins R. LIVE/DEAD BacLight : application of a new rapid staining method for direct enumeration of viable and total bacteria in drinking water. *J Microbiol Methods.* 1999;37(1):77-86.



Acoustofluidic Separation of Oblate Spheroid from Sphere using Acoustic Radiation Torque and Force

View Article Online
DOI: 10.1039/C6LC00140H

Muhammad Soban Khan,¹ Mushtaq Ali,¹ Yong Bin Bang,² Seong Jae Lee^{2,*} and Jinsoo Park^{1,*}

¹Department of Mechanical Engineering, Chonnam National University, 77 Yongbong-ro, Buk-gu, Gwangju 61186, Republic of Korea

²Department of Polymer Engineering, The University of Suwon, 17 Wauan-gil, Bongdam-eup, Hwaseong, Gyeonggi 18323, Republic of Korea

*Correspondence: Jinsoo Park (jinsoopark@jnu.ac.kr) and Seong Jae Lee (sjlee@suwon.ac.kr)

Data availability

All data reported in this work are available from the corresponding author upon reasonable request.

The supplementary information (SI) associated with this article includes: derivation of the acoustic radiation torque and force along with radiation force function (Y_p); numerical investigation of asymmetric wave scattering from oblate spheroids with varying orientation and aspect ratio; acoustic radiation force factor (F_F) graphs with varying acoustic wave frequency (f) and the PS particle and RBCs diameter (d_p) (Fig. S1); Fig. S2 (supporting experimental results for Fig. 6); Fig. S3 shows S_{11} measurement data of both IDTs by a vector network analyzer; Fig. S4 indicates roles of ART and ARF in particle orientation and particle vertical migration. Supplementary Movie 1 (illustrating movement of spherical and oblate particle in an acoustic field).

